

AD-A079 551

ARTEC ASSOCIATES INC HAYWARD CALIF
EXPLOSIVE MHD RESEARCH.(U)
MAY 77 S P GILL, D W BAUM, W L SHIMMIN
FR-119

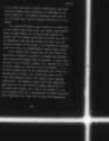
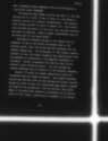
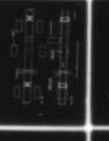
F/G 10/2

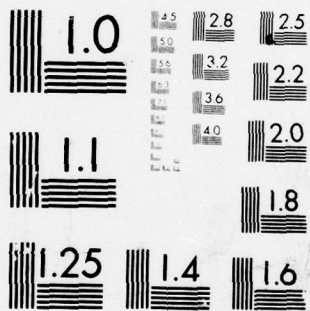
UNCLASSIFIED

N00014-75-C-0822

NL

1 OF 2
AD
A079551





MICROCOPY RESOLUTION TEST CHART
NATIONAL BUREAU OF STANDARDS-1963-A


ADA079551

LEVEL *12*



DDC
REF ID: A66112
JAN 16 1980
RESERVED

DDC FILE COPY

ARTEC 
ASSOCIATES INC

This document has been approved
for public release and sale; its
distribution is unlimited.

80 1 14 093

12

6 EXPLOSIVE MHD RESEARCH,

9 Final Report 119
Period: 1 Apr 1976 to
31 Mar 1977,

DDC
RECEIVED
JAN 10 1980
E

14 FR-119

Sponsored by: Office of Naval Research
Requisition Authority No. 099-406/1-8-75
Contract No. N00014-75-C-0822

15

By: 10 Stephen P./Gill, Dennis W./Baum,
W. Lee/Shimmin, E./Mukherjee
ARTEC ASSOCIATES INCORPORATED
26046 Eden Landing Road
Hayward, California 94545
Telephone: (415) 785-8080

Deb

11 31 May 77

12 125

Reproduction in whole or in part is permitted for
any purpose of the United States Government.

408 296

This document has been approved
for public release and sale; its
distribution is unlimited.

mt

UNCLASSIFIED

SECURITY CLASSIFICATION OF THIS PAGE (When Data Entered)

REPORT DOCUMENTATION PAGE		READ INSTRUCTIONS BEFORE COMPLETING FORM
1. REPORT NUMBER FR-119	2. GOVT ACCESSION NO.	3. RECIPIENT'S CATALOG NUMBER
4. TITLE (and Subtitle) "EXPLOSIVE MHD RESEARCH"		5. TYPE OF REPORT & PERIOD COVERED Final Report 1 APR 76 to 1 APR 77
		6. PERFORMING ORG. REPORT NUMBER
7. AUTHOR(s) S. P. Gill, D. W. Baum, W. L. Shimmin, and D. Mukherjee		8. CONTRACT OR GRANT NUMBER(s) N00014-75-C-0822
9. PERFORMING ORGANIZATION NAME AND ADDRESS ARTEC ASSOCIATES INCORPORATED 26046 Eden Landing Road Hayward, California 94545		10. PROGRAM ELEMENT, PROJECT, TASK AREA & WORK UNIT NUMBERS 61153N
11. CONTROLLING OFFICE NAME AND ADDRESS Office of Naval Research Department of the Navy Code 613A:TB 800 N. Quincy St., Arlington, Va. 22217		12. REPORT DATE 31 MAY 77
		13. NUMBER OF PAGES 122
14. MONITORING AGENCY NAME & ADDRESS (if different from Controlling Office)		15. SECURITY CLASS. (of this report) UNCLASSIFIED
		15a. DECLASSIFICATION/DOWNGRADING SCHEDULE
16. DISTRIBUTION STATEMENT (of this Report) <div style="border: 1px solid black; padding: 5px; margin: 10px auto; width: fit-content;">This document has been approved for public release and sale; its distribution is unlimited.</div>		
17. DISTRIBUTION STATEMENT (of the abstract entered in Block 20, if different from Report)		
18. SUPPLEMENTARY NOTES		
19. KEY WORDS (Continue on reverse side if necessary and identify by block number) Magnetohydrodynamics, Plasma, Energy Conversion, Explosive MHD, Explosive Driver		
20. ABSTRACT (Continue on reverse side if necessary and identify by block number) Research on dense nonideal plasmas used in explosive MHD pulse power generators is described. Experiments were performed with three types of explosive plasma sources producing a plasma pressure about 10 kbar and a plasma temperature about 5 eV (58,000° K). A literature survey was performed on theoretical methods for predicting the properties of nonideal plasmas, and calculations were performed using some of the models. Encouraging progress was made in reducing a discrepancy between theory and experiment.		

DD FORM 1 JAN 73 1473

EDITION OF 1 NOV 65 IS OBSOLETE

-1-

UNCLASSIFIED

SECURITY CLASSIFICATION OF THIS PAGE (When Data Entered)

PREFACE

The work presented in this report was performed at Artec Associates Incorporated, Hayward, California. Dr. Stephen P. Gill and Dr. Dennis W. Baum were the principal investigators; Mr. W. Lee Shimmin carried out the experimental effort; and Dr. Deb Mukherjee carried out the theoretical effort. The work was performed under the auspices of the Office of Naval Research with Mr. J. A. Satkowski as technical monitor.

Accession For	
NTIS GRA&I	<input checked="" type="checkbox"/>
DDC TAB	<input type="checkbox"/>
Unannounced	<input type="checkbox"/>
Justification	<i>for</i>
<i>from 50 on file</i>	
By	
Distribution/	
Availability Code	
Dist	Available/or special
<i>A</i>	

TABLE OF CONTENTS

	<u>Page</u>
DD FORM 1473	1
PREFACE.	2
LIST OF FIGURES.	4
LIST OF TABLES	6
1. INTRODUCTION AND BACKGROUND.	7
1.1 Explosive MHD Generators.	7
1.2 Explosive Plasma Source Data.	7
1.3 Explosive MHD Data.	9
1.4 Need for Better Understanding of Nonideal Plasmas.	11
1.5 Research Program Plan	12
2. EXPERIMENTAL PROGRAM	13
2.1 Objectives and Experimental Plan.	13
2.2 Description of Explosive Driver Plasma Sources.	14
2.3 Experimental Driver Performance	20
2.4 Diagnostic Channel.	30
2.5 Design of Plasma Diagnostics.	31
2.6 Experimental Results.	48
3. THEORETICAL PROGRAM.	83
3.1 Purpose	83
3.2 Ideal Plasma Calculations	83
3.3 Debye-Huckel Calculations	85
3.4 Parameters Characterizing Plasma Regime.	91
3.5 Survey of Current Research in Nonideal Plasmas	97
3.6 Conclusions of Theoretical Program.	110
3.7 Preliminary Estimates of Explosive Plasma Conductivity	112
4. CONCLUSIONS AND RECOMMENDATIONS.	117
4.1 Summary of Program Accomplishments.	117
4.2 Recommendations	117
REFERENCES	119

LIST OF FIGURES

<u>Figure</u>		<u>Page</u>
2.1	Cylindrical Imploding Driver	16
2.2	Cylindrical Exploding Driver	16
2.3	Disc Exploding Driver.	18
2.4	Field Photographs of Drivers Used on Experimental Program	22
2.5	Position-Time for Imploding Cylinder Type Driver, Shot 119-23	23
2.6	Field Photograph of Disc Type Driver Used on Shot 119-19.	24
2.7	Position-Time Diagram for Disc Type Driver, Shot 119-20.	26
2.8	Position-Time Diagram for Exploding Cylinder Type Driver, Shot 119-21.	27
2.9	Position-Time Diagram for Exploding Cylinder Type Driver, Shot 119-22.	28
2.10	Brass Velocity Gage Electrode Configuration.	33
2.11	End View of Load Circuit Configuration	33
2.12	Illustration of Eddy Currents Arising in Plasma Flow Due to Magnetid Field Gradient	37
2.13	Conductivity Gage Laboratory Calibration Curve for Gage No. 1, Shot 119-23.	39
2.14	Geometrical Layout of Optical Pyrometer.	42
2.15	Basic Channel Layout for Shots 119-17 thru -20	45
2.16	Lab Photographs of Typical Diagnostic Channel Assembly	46
2.17	Basic Channel Layout for Shots 119-21 and -22.	47
2.18	Basic Channel Layout for Shot 119-23	49
2.19	Velocity Gage and Load Monitor Records for Shot 119-17.	50
2.20	Conductivity Gage Records for Shot 119-17.	51
2.21	Velocity Gage and Load Monitor Records for Shot 119-18.	52
2.22	Conductivity Gage Records for Shot 119-18.	53
2.23	Ideal Load Voltage and Current Waveforms for Constant Flow Velocity and Plasma Resistance	55
2.24	Velocity Gage and Load Monitor Records for Shot 119-20.	58
2.25	Conductivity Gage Output Versus Time for Shot 119-20.	59

LIST OF FIGURES (Continued)

<u>Figure</u>		<u>Page</u>
2.26	Plots of Experimental Results on Shot 119-20.	61
2.27	Results of Lab Test of Conductivity Gage Response Variations with Bar Diameter	64
2.28	Load Monitor Records for Shot 119-21	67
2.29	Conductivity Gage Output Versus Time for Shot 119-21.	68
2.30	Load Monitor Records for Shot 119-22	69
2.31	Conductivity Gage and Optical Pyrometer Records for Shot 119-22.	70
2.32	Typical Ablation Pattern Observed on Load Electrodes.	74
2.33	Velocity Gage and Optical Pyrometer Records for Shot 119-23.	76
2.34	Conductivity Gage Records for Shot 119-23. . .	77

LIST OF TABLES

<u>Table</u>		<u>Page</u>
1.1	Experimental Data on Explosively Driven Plasma Source.	8
1.2	Experimental Data on Explosive MHD Power Generation.	10
2.1	Summary of Experiments Performed.	15
2.2	Summary of Experimental Performance of Drivers.	29
2.3	Summary of Conductivity Measurements.	80
3.1	Results of Plasma Calculations for 10 kbar Xenon Driver Conditions	86
3.2	Calculated Plasma Length Scales for 10 kbar Xenon Driver Conditions	95
3.3	Calculated Dimensionless Plasma Parameters for 10 kbar Xenon Driver Conditions.	96
3.4	Summary of Research on Thermodynamics of Nonideal Plasmas	98
3.5	Summary of Research on Electrical Conductivity of Nonideal Plasmas.	106
3.6	Preliminary Estimates of Electrical Conductivity 10 kbar Xenon Driver	114

1. INTRODUCTION AND BACKGROUND

1.1 Explosive MHD Generators

Explosively driven MHD generators, as described in References 1.1 to 1.3, operate by using an intermediary gas to transform explosive energy to useful electrical output. Detonating explosive is used to shock-compress and energize argon or xenon gas to a dense, high temperature, electrically conducting plasma. When this plasma is passed through a magnetic field, electric power is generated.

Energy stored in an explosive is enormous by electrical standards. Octol explosive, for example, contains approximately 2.4 megajoules chemical energy per pound of explosive. Even at the present state of the art, and much remains to be done, over 10% of the chemical energy is transferred to the intermediary plasma.

1.2 Explosive Plasma Source Data

A summary of recent experimental data on explosively driven plasma sources is shown in Table 1.1. The data includes the results of the present program together with results described in References 1.1 to 1.3. It should be noted that there is no direct method for measuring the energy output of an explosive driver, and performance must be inferred from shock wave measurements as described in Section 2.3 below. Because of the variety of plasma pulse

TABLE 1.1
EXPERIMENTAL DATA ON EXPLOSIVELY DRIVEN PLASMA SOURCE

Shot No.	Description	Composition	Driver Plasma Velocity (km/sec)	Driver Pulse Duration (μsec)	Nominal Driver Pressure (kilobar)	Specific Energy (joules/g)	Total Enthalpy (joules)	Average Thermal Power (watts)
113-1, -3 -5, -6 -8, -9, thru -13	Disc Driver: Before Reflection Output	Argon	10 avg. 11 peak	6 25	15 avg. 2.2 peak	5.0x10 ⁴	2.3x10 ⁶	3.8x10 ¹¹
113-2	Asymmetric Disc: Before Reflection Output	Argon	12 avg. 16 peak	-- 14	23 avg. 4.8 peak	7.2x10 ⁴	3.2x10 ⁶	--
113-14 & 119-16	Imploding Cylinder	Xenon	8.5	25	10	3.6x10 ⁴	1.5x10 ⁶	6.0x10 ¹⁰
119-17	Imploding Cylinder	Argon	8.5	21	10	3.6x10 ⁴	7.6x10 ⁵	3.6x10 ¹⁰
119-18 & 119-23	Imploding Cylinder	Xenon	8.5	21	10	3.6x10 ⁴	7.6x10 ⁵	3.6x10 ¹⁰
119-19 & 119-20	Disc Driver: Before Reflection Output	Xenon	10.5 avg. 11 peak	6 30	15 avg. 2.2 peak	5.5x10 ⁴	2.5x10 ⁶	4.2x10 ¹¹
119-21	Exploding Cylinder	Argon	8.5	13	6	3.6x10 ⁴	3.7x10 ⁶	2.8x10 ¹¹
119-22	Exploding Cylinder	Xenon	8.5	11	6	3.6x10 ⁴	3.2x10 ⁶	2.9x10 ¹¹
120-1	Exploding Cylinder	Argon	8.5	10	10	3.6x10 ⁴	4.8x10 ⁶	4.8x10 ¹¹
120-2	Exploding Cylinder	Argon	8.5	14	6	3.6x10 ⁴	4.4x10 ⁶	3.1x10 ¹¹
120-3	Exploding Cylinder	Xenon	8.5	10	6	3.6x10 ⁴	3.0x10 ⁶	3.0x10 ¹¹
120-4	Exploding Cylinder	Xenon	8.5	16	6	3.6x10 ⁴	9.9x10 ⁶	6.2x10 ¹¹

shapes and the existence of several nonideal phenomena occurring in explosive driver operation (such as tube expansion, boundary layers, etc.) the data in Table 1.1 are to be considered nominal values only. Actual values, if they could be measured, might deviate by as much as 50% from the nominal values.

Since explosive drivers deliver several megajoules of plasma energy in a few tens of microseconds, the average thermal power level is very high, on the order of 10^{11} watts (100 gigawatts). To transform this plasma power to electrical power in an MHD generator requires intense magnetic fields, from 10 to 50 tesla. At these field levels the magnetic pressures are comparable to the plasma pressure. The intense fields are required only in the MHD channel, which is about 2.5-cm diameter by 10-cm long.

1.3 Explosive MHD Data

A summary of experimental data on the electrical performance of explosive MHD generators is shown in Table 1.2 (References 1.1 to 1.3). Peak power is principally limited by magnetic field strength which ranged from a 0.1 tesla permanent magnet to a 3.6 tesla self-excited field. Delivered power varies approximately as the square of the magnetic field.

The most practical method for achieving high values of

TABLE 1.2
EXPERIMENTAL DATA ON EXPLOSIVE MHD POWER GENERATION

Shot	Description	Field Source	Peak Field (Tesla)	Load	Peak Power (Watts)	Comments
113-5	Disc Driver plus Reservoir	Permanent Magnet	0.10	11 mΩ Resistor	9x10 ³	
113-4	Disc Driver plus Reservoir	Permanent Magnet	0.10	45 nH Inductor	3.6x10 ³	
113-9	Disc Driver plus Reservoir	Electromagnet	0.9	11 mΩ Resistor	1.6x10 ⁵	
113-10	Disc Driver	Electromagnet	0.8	5 mΩ Resistor	2.1x10 ⁶	
113-14	Imploding Cylinder plus Reservoir	1 Tesla Electro-magnet plus self-excitation	1.6	140 nH Inductor	4.4x10 ⁶	
119-16	Imploding Cylinder	Electromagnet	0.7	10 mΩ Resistor	2.1x10 ⁶	
120-1	Exploding Cylinder	Electromagnet	0.6	2 mΩ Resistor	1.1x10 ⁶	
120-2	Exploding Cylinder	Electromagnet	0.6	2 mΩ Resistor	9.5x10 ⁵	
120-3	Exploding Cylinder	Electromagnet	0.9	144 nH Inductor 1.4 mΩ Resistor	9.9x10 ⁶ 4.6x10 ⁶	Two-stage
120-4	Exploding Cylinder	0.4 Tesla Electromagnet plus self-excitation	3.6	70 nH Inductor	6.2x10 ⁷ ea 3.1x10 ⁸ tot	Five-stage

the magnetic field strength in single-shot explosive devices is self-excitation. A small initial field (.1 to .3 tesla) is provided from a permanent magnet, and power from this field is used to amplify the field strength to full operational values.

1.4 Need for Better Understanding of Nonideal Plasmas

Recent self-excitation experiments (References 1.2 and 1.3) have uncovered a serious discrepancy between theory and experiment with regard to plasma resistance, ranging from a factor of three to a factor of ten. This discrepancy has been the principal technical problem preventing the achievement of full self-excitation of an explosive MHD generator in recent experiments.

Explosively driven plasmas are characterized by extremely high pressures, energies, and velocities compared with more conventional plasma sources. Although the conditions are well suited to MHD power production, they are remarkably difficult for theoretical analysis and accurate experimental diagnostics. The plasma is fully ionized and optically dense, so that most electrical and optical instrumentation techniques developed for thin plasmas are not appropriate. All measurements are made in an explosive test environment, with destruction of most test components in every shot. Theoretically, calculation of explosive plasma

properties represents a challenge because of the density; free charges are packed so close together that they resemble a metallic solid as much as a plasma.

1.5 Research Program Plan

At the outset of this program, having received experimental data demonstrating serious problems regarding the prediction of explosively driven plasmas (Reference 1.2), it was decided to concentrate all the effort on achieving a better scientific understanding of dense nonideal plasmas.

To this end a combined experimental and theoretical effort was planned. The experimental program, described in Section 2 below, concentrated on making experimental measurements of the driver plasma directly as it exited the explosive driver. This approach eliminated extraneous interactions with the MHD channel which might affect results, and yielded the most well-determined plasma possible from the explosive driver. The theoretical program, described in Section 3, was concerned with surveying world literature in nonideal plasma theory, and achieving a deeper understanding of the physical phenomena relevant to explosive driver conditions.

The results of this effort are encouraging, as discussed in Section 4, and it is probably safe to say that quantitative agreement between experiment and theory are well within sight.

2. EXPERIMENTAL PROGRAM

2.1 Objectives and Experimental Plan

The primary purpose of the experimental program was to perform diagnostic experiments on high density plasmas produced by explosive drivers. The principal diagnostic techniques selected for this purpose were an MHD plasma velocity gage, an electrode-to-electrode plasma resistance measurement, an electrodeless conductivity gage utilizing magnetic pickup of eddy currents, shock wave parameter measurements, and a band-limited optical pyrometer to monitor surface brightness temperature of the plasma.

Three different types of explosive drivers were used to determine whether the mode of plasma production affected bulk properties. The principal concern was the possibility of contaminants being jetted or ablated into the plasma during driver operation. The three driver types -- imploding cylinder, exploding cylinder, and disc -- have such widely differing modes of operation that it is unlikely for the degree of plasma contamination to be the same, and a comparison of measured plasma properties was expected to indicate whether contamination is responsible for the observed low electrical conductivity.

Two driver gases, argon and xenon, were selected for the test series. Theory predicts substantially different temperature and electrical conductivity for these two gases

in an explosive driver, and this difference may be tested by direct experimental measurement.

The original experimental plan was to fire one shot for each of the two gases in each of the three types of driver using the same diagnostic channel. Constraints of time, contract resources, and diagnostic development problems modified this plan somewhat, but much of the expected data was obtained. Table 2.1 describes the main features of the experiments that were performed.

2.2 Description of Explosive Driver Plasma Sources

Each of the three types of explosive driver -- cylindrical imploding, cylindrical exploding, and disc -- transfers explosive energy to a dense high pressure plasma by means of a strong shock wave, but does so with differing geometrical configurations and modes of plasma processing.

The cylindrical imploding driver is shown in Figure 2.1. Detonating explosive progressively collapses a tube containing the driver gas. The imploding tube provides a cone-shaped gas seal translating axially at a velocity equal to the detonation velocity of the explosive, which for our experiments is 8.5 km/sec ($.85 \text{ cm}/\mu\text{sec}$). The effect of this seal is to provide a piston driving a strong shock wave into the driver gas, which pressurizes and energizes the plasma. Energy is transferred from the explosive to the plasma by

TABLE 2.1
SUMMARY OF EXPERIMENTS PERFORMED

Shot No.	Driver Type	Plasma Composition	Nominal Driver Pressure (kilobar)	Channel Plasma Velocity (km/sec)	Channel Pulse Duration (μ sec)	Velocity Gage	Plasma Resistance	Conductivity Gages	Optical Pyrometer
119-17	Imploding Cylinder	Argon	10	8.5	25	X	X	XX	
119-18	Imploding Cylinder	Xenon	10	8.5	25	X	X	XX	
119-19	Disc	Xenon	10	12	25	X	X	X	
119-20	Disc	Xenon	10	12	25	X	X	X	
119-21	Exploding Cylinder	Argon	6	9.5	35	X	XX	X	X
119-22	Exploding Cylinder	Xenon	6	8.6	35	X	XX	X	X
119-23	Imploding Cylinder	Xenon	10	8.5	25	X		XXX	X

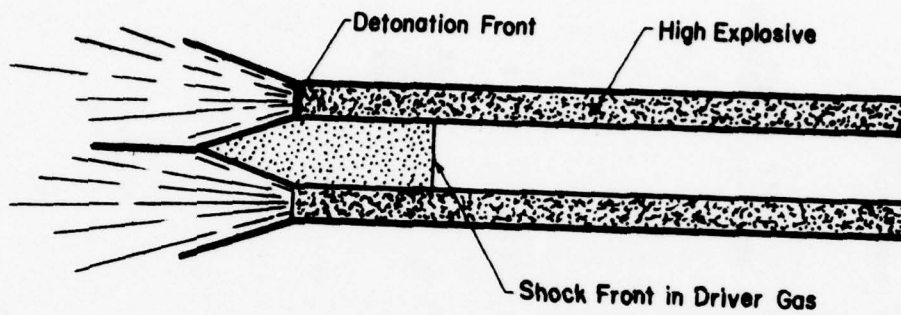


Figure 2.1 Cylindrical Imploding Driver

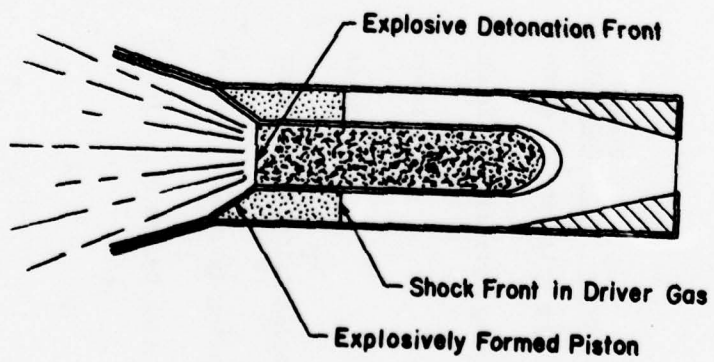


Figure 2.2 Cylindrical Exploding Driver

virtue of the fact that the imploding tube must do work to collapse against the pressure of shocked driver gas, which in our experiments was approximately 10 kilobars. The cylindrical imploding driver represents the most ideal plasma processing, since it is essentially a constant area shock tube with constant velocity piston.

The cylindrical exploding driver is shown in Figure 2.2. It differs from the imploding driver in that the locations of explosive and driver gas are reversed, and the detonating explosive expands a tube to seal against an outer tube. The moving gas seal drives a strong shock into the annulus containing the driver gas, and energy is transferred by the expanding tube doing work against the shock pressure. Efficiency of the exploding tube is much greater than the imploding tube, but the gas seal is more difficult because it is a line seal rather than a point seal. The cylindrical exploding driver also requires a transition section to process the high pressure plasma from an annular driver tube to a cylindrical MHD channel.

The disc explosive driver shown in Figure 2.3 uses the exploding driver principle to drive a radially converging shock wave into the driver gas. The resulting plasma stagnates at the axis and expands into the MHD channel. The disc driver is both efficient and compact, but involves more complex plasma processing than either of the cylindrical types.

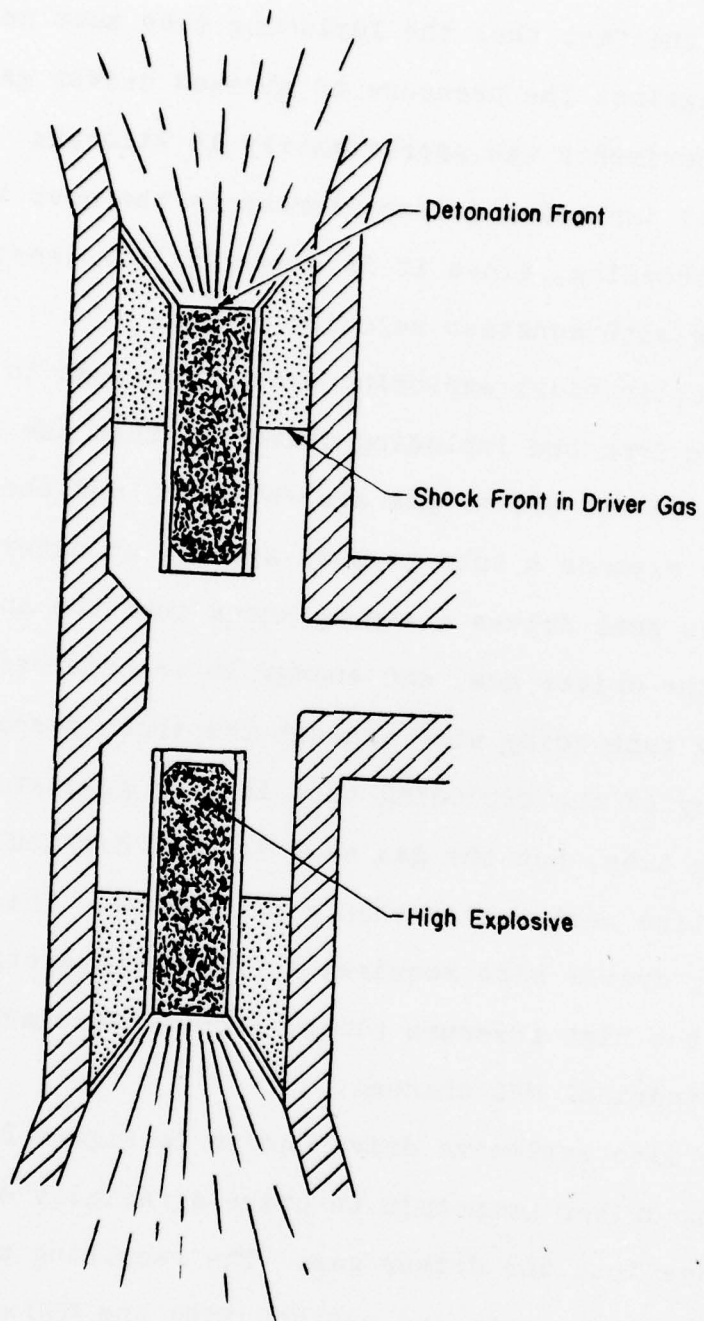


Figure 2.3 Disc Exploding Driver

Modes of potential plasma contamination are different for each of the driver types. The imploding driver has a potential jetting problem, similar to a shaped charge device, in which a jet of tube wall material is thrown forward from the collapse point into the plasma. The jet can be minimized and theoretically eliminated by proper design of driver parameters, but there is no known method for monitoring driver operation to assure absence of small quantities of jet contamination. Jetting is much less of a problem in the impact regions of the cylindrical exploding driver and the disc driver, since jetting is easier to suppress in a line impact than it is in a radially converging point impact of a metal tube.

Ablation from the driver tube materials by the driver plasma is another source of contamination. The cylindrical imploding driver is expected to have least ablative contamination because of the simple flow geometry and minimum wall exposure to the flowing plasma. The cylindrical exploding driver is potentially worse because of the transition section, in which the plasma may ablate material from the converging nozzle walls. Plasma in the disc driver first stagnates, then expands down an MHD channel, which may lead to more ablation than would be expected from the straight-through flow of the cylindrical imploding driver.

Energetic performance of the driver and plasma thermodynamic state are also affected by the driver type. The simplest situation is the cylindrical imploding driver, in which the plasma is processed by a single planar shock at constant velocity. The cylindrical exploding driver adds the complication of gas processing and expansion in the transition section. The disc driver has a variable velocity shock in the disc, and the plasma is subsequently stagnated and reexpanded.

2.3 Experimental Driver Performance

Driver gas is energized and compressed to a dense plasma state by a strong shock wave, and the principal means of assessing mechanical performance of the driver and estimating plasma energy is by monitoring the location and velocity of the shock wave.

The Hugoniot shock jump relationships expressing conservation of mass, momentum, and energy across the shock front yield the following relationships for plasma pressure and energy:

$$p = \rho_0 u U_s \quad (2.1)$$

$$e = \frac{1}{2} u^2 \quad (2.2)$$

Here ρ_0 is initial loading density of the driver gas, u is the plasma flow velocity, and U_s is the shock velocity. Flow velocity is related to shock velocity by the relationship

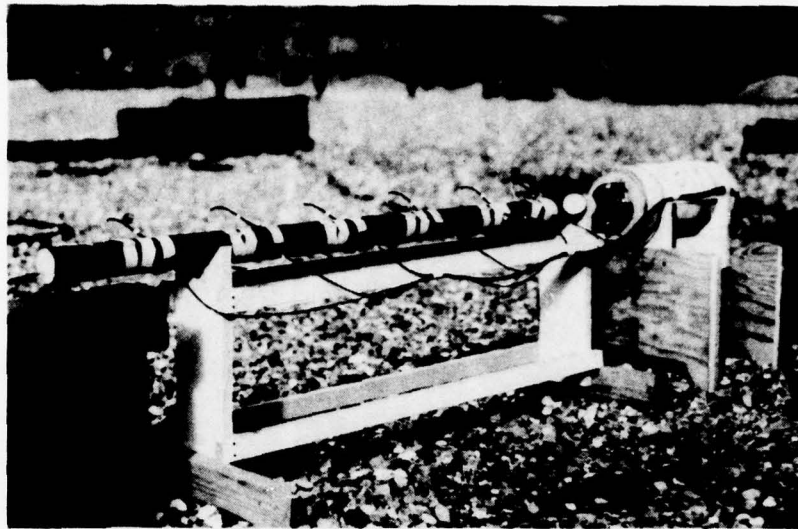
$$u = \left(1 - \frac{\rho_0}{\rho}\right) U_s \quad (2.3)$$

where ρ is the shock-compressed density of the plasma.

Shock location and velocity are monitored by capped pins short-circuited by the shock pressure pulse. Detonation location is monitored by ionization pins placed against the explosive, with ionization phenomena in the detonation short-circuiting the pins. The pins are connected to a ladder network of R-C circuits, so that short-circuiting a pin generates a coded data point monitored on an oscilloscope.

Shots 119-17, -18, and -23 were all imploding cylinder type drivers (see Figure 2.4 (a)). All the shots performed similarly, and an $x-t$ diagram of Shot 119-23 is shown in Figure 2.5 as an example. The driver shock velocity is .893 cm/ μ sec, about 7% lower than ideal (.96 cm/ μ sec) based on measured detonation velocity. It is likely that non-ideal factors such as tube wall expansion and boundary layer effects contribute to this difference.

Shots 119-19 and 119-20 were both disc type drivers (see Figure 2.6). The $x-t$ diagram for Shot 119-20 is shown



a) Imploding Cylinder Type Driver, Shot 119-17



b) Exploding Cylinder Type Driver, Shot 119-21

Figure 2.4 Field Photographs of Drivers Used on Experimental Program

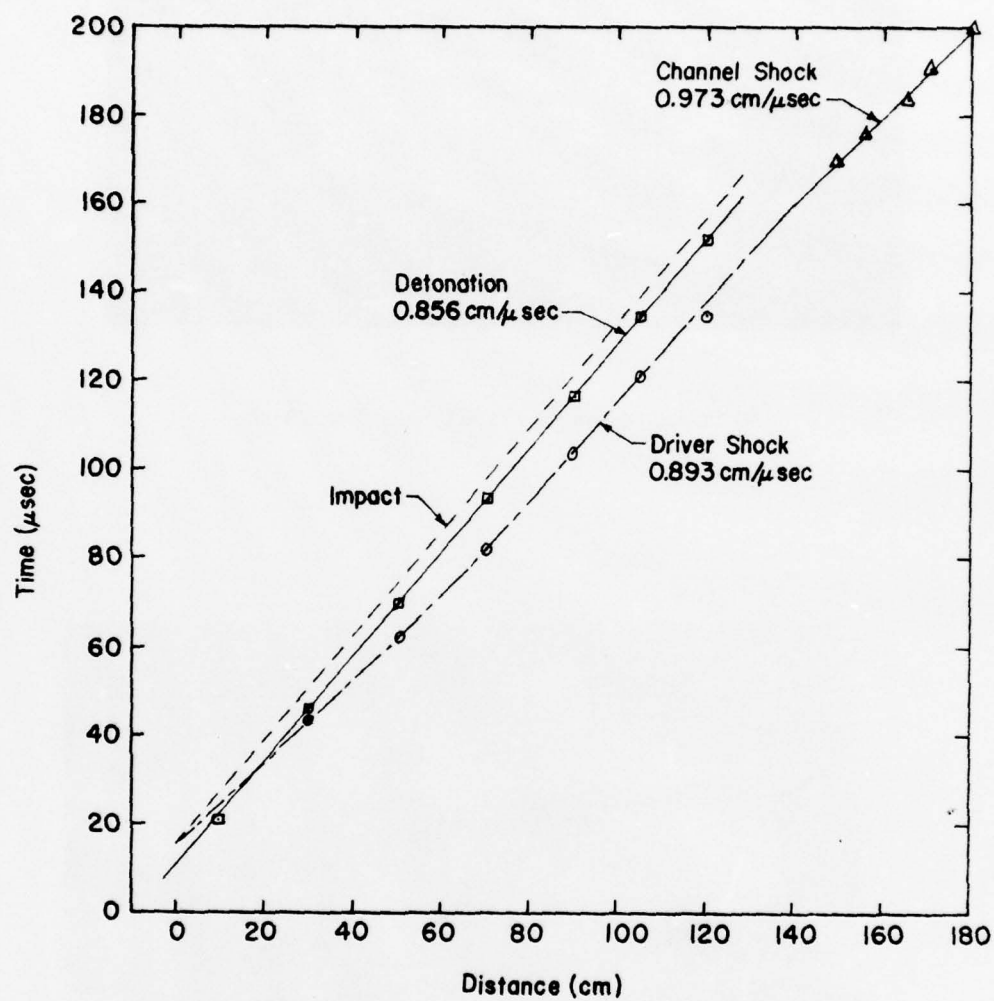


Figure 2.5 Position-Time Diagram for Imploding Cylinder Type Driver, Shot 119-23

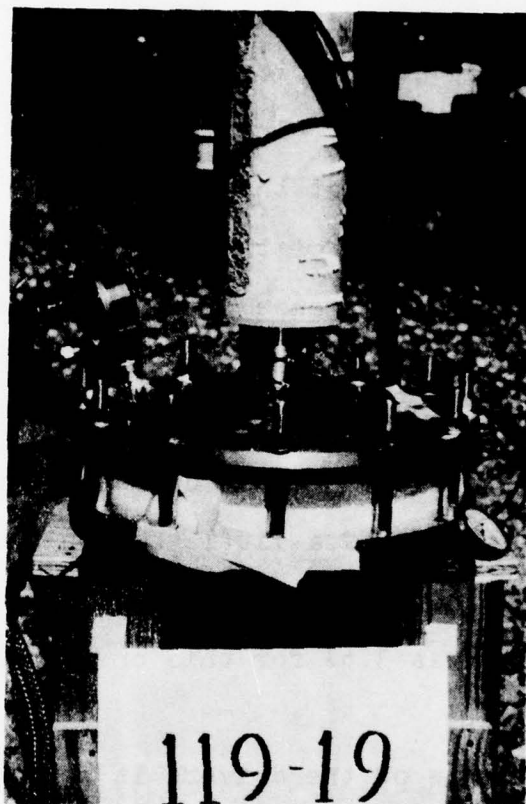


Figure 2.6 Field Photograph of Disc Type Driver Used on Shot 119-19

in Figure 2.7, indicating the shock acceleration caused by radial convergence.

Shots 119-21 and -22 were both exploding cylinder type drivers (see Figure 2.4(b)). Their $x-t$ diagrams, shown in Figures 2.8 and 2.9, indicate a slowdown in growth of the shocked plasma region. This result is most likely caused by gas seal problems at the impact point, a problem observed previously on drivers of this type. Evidence to date indicates that the performance of cylindrical exploding drivers is noticeably dependent on the circumferential uniformity of the aluminum expansion tube wall thickness. In keeping with this observation it can be seen that the driver on Shot 119-21 performed a little better than the other one. The measured initial wall thickness variation around the circumference was 3.6% for this one as compared with 5.9% for the other.

Performance of the drivers is summarized in Table 2.2. Using measured shock velocity and known initial conditions, shock pressure and energy immediately behind the shock front are calculated. These values typically are less than the nominal value based on ideal driver operation, because the shock velocity is typically less than ideal by a few percent, and both pressure and energy depend on the square of the velocity.

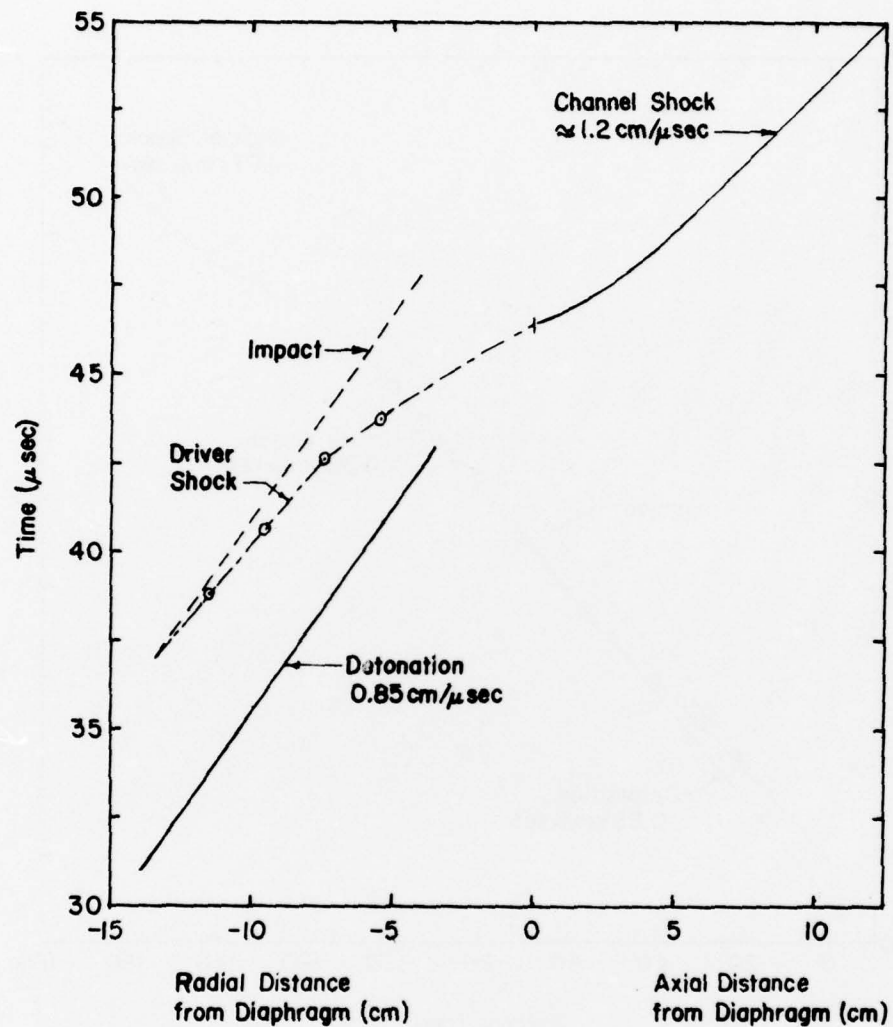


Figure 2.7 Position-Time Diagram for Disc Type Driver, Shot 119-20

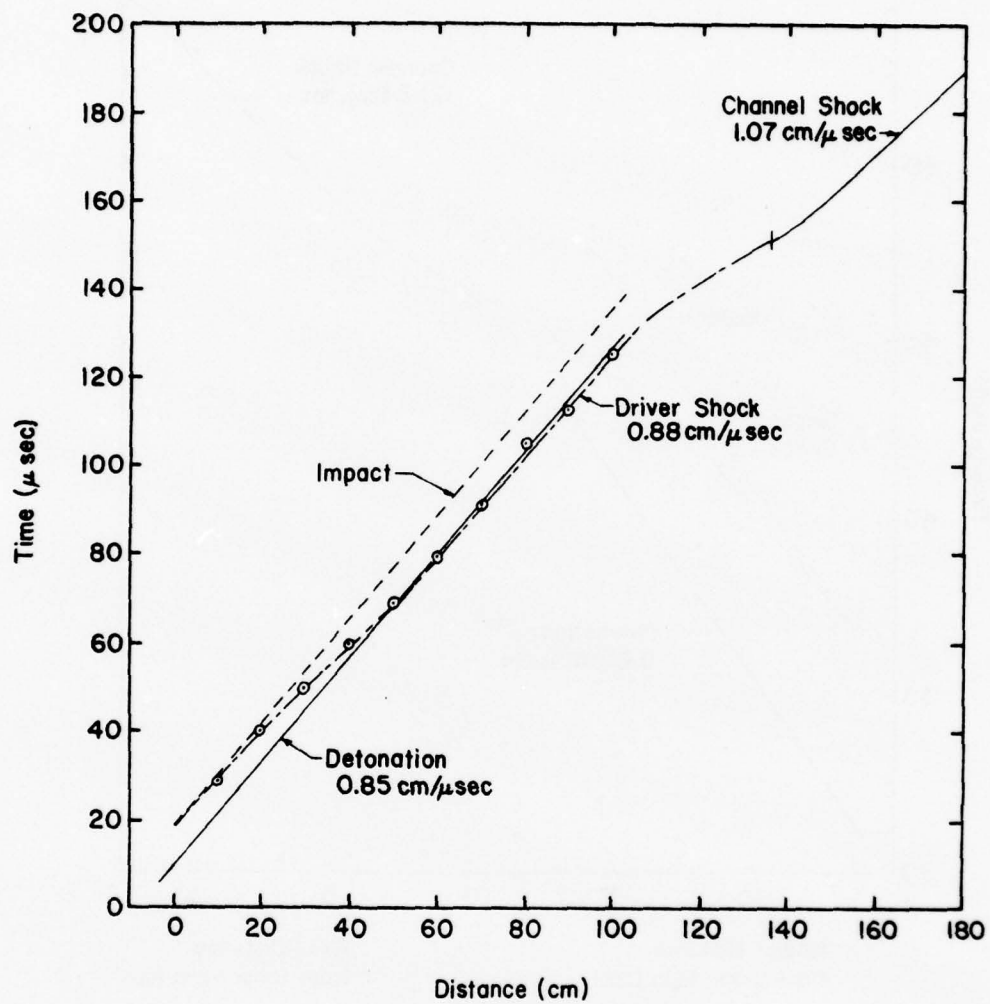


Figure 2.8 Position-Time Diagram for Exploding Cylinder Type Driver, Shot 119-21

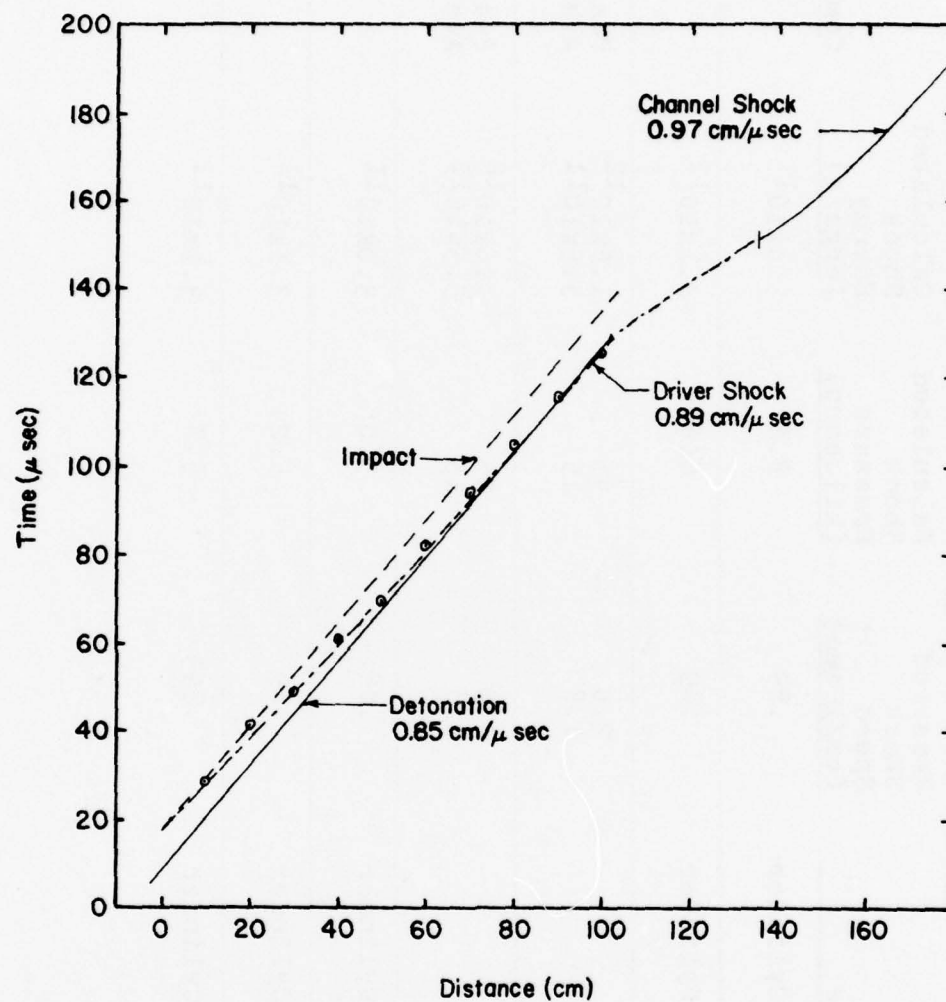


Figure 2.9 Position-Time Diagram for Exploding Cylinder Type Driver, Shot 119-22

TABLE 2.2
SUMMARY OF EXPERIMENTAL PERFORMANCE OF DRIVERS

<u>Shot No.</u>	<u>Driver Type</u>	<u>Measured Shock Speed (cm/μ sec)</u>	<u>Calculated Shock Pressure (kilobars)</u>	<u>Calculated Shock Energy (ergs/g)</u>	<u>Comments</u>
119-17	Imploding Cylinder	.89	8.6	3.0×10^{11}	
119-18	Imploding Cylinder	.89	8.6	3.1×10^{11}	
119-19	Disc	2.0 1.8	45 15	1.6×10^{12} 5.5×10^{11}	Peak Average
119-20	Disc	2.0 1.8	45 15	1.6×10^{12} 5.5×10^{11}	Peak Average
119-21	Exploding Cylinder	.88	5.0	3.0×10^{11}	
119-22	Exploding Cylinder	.89	5.2	3.1×10^{11}	
119-23	Imploding Cylinder	.893	8.7	3.1×10^{11}	

2.4 Diagnostic Channel

A one-inch-diameter diagnostic channel was used on all experiments. Channel material was Lexan (polycarbonate resin manufactured by General Electric Co.), a one-inch I.D. tube with 1/8-inch wall thickness. Since ablation products affect electrical conductivity, some effort was initially expended in investigating alternate channel materials. Glass (silicon dioxide) appeared favorable, because the silicon ablation products tend to maintain high electrical conductivity, but practical fabrication problems led to discontinuation of the effort. Calculations indicate that the Lexan ablation products reduce plasma conductivity in the boundary layer mixing region, and it was anticipated that experiments might tend to confirm this effect.

On the shots using the imploding cylinder type driver the channel was mounted as an extension of the driver pressure tube, designed to have a one-inch I.D. The system was pressurized to give a nominal 10 kilobar shock pressure, and consequently the channel required considerable tamping to prevent significant wall motion during approximately 20 μ sec of measurements. To provide this tamping the assembled diagnostic channel was cast in Hydrostone (a high density plaster, $\rho = 1.76 \text{ g/cm}^3$) filled with #9 lead shot. The mixture was vibrated during filling to achieve a high packing density of the shot. This type of tamper was used on all the diagnostic channels.

On the shots using the disc type driver the channel was mounted to the driver with a .001-inch-thick steel diaphragm interposed. The channel had a one-atmosphere argon background gas, and the driver shock expanded into this gas. A longer duration pressure profile is obtained in this way, thus simplifying the process of relating measurements made at different axial locations.

On the shots using the exploding cylinder type driver the ring of shocked gas produced by the driver gas was passed through a long (13-inch) tapered section (8 degree taper) and then through a steel diaphragm into the one-inch diameter channel. In addition to using one-atmosphere argon as a background gas in the channel, the first 18 inches of the channel consisted of a steel barrel to allow further runout or stretching of the plasma pulse.

2.5 Design of Plasma Diagnostics

2.5.1 MHD Velocity Gage

The velocity gage operates as an open circuit Faraday MHD generator where the voltage is given by the equation

$$V_o = B u b \quad (2.4)$$

where B is magnetic field strength, u is plasma flow velocity, and b is the interelectrode spacing. With a known magnetic

field and known electrode spacing the measured voltage provides the plasma velocity history by

$$u(t) = \frac{V_o(t)}{Bb} \quad (2.5)$$

All diagnostic channels used a velocity gage with barium ferrite permanent magnets providing the magnetic field (typically $B \approx 0.1$ tesla). In all cases a pair of 0.2-inch diameter brass electrodes protruded 0.1 inch into the channel (see Figure 2.10) giving a spacing of 0.8 inches.

The electrodes were attached to a coaxial cable, and the output was viewed across a 50Ω terminating resistor at the scope. Since the gas resistance is $\sim 10^{-2}$ ohm, the 50 ohm termination was essentially open circuit.

Since the magnets do not produce an uniform B-field throughout the volume of interest a procedure was devised to obtain the effective B-field,

$$B_{eff} = \frac{V_o}{ub} \quad (2.6)$$

A spring driven aluminum bar was used to simulate the plasma. It was propelled through a Lexan tube similar to the channels, and it had a pair of magnets set up similarly to the shot geometry. A pair of stranded wires were used as brush contacts for measuring the voltage across the bar diameter in

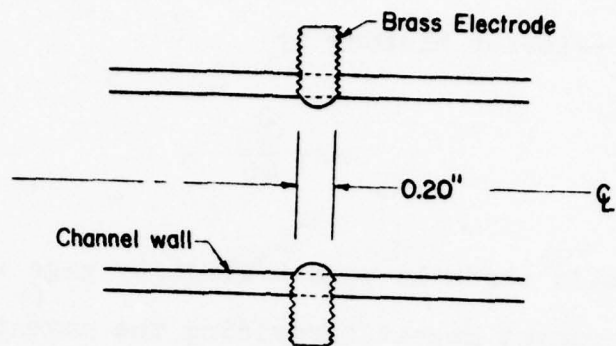


Figure 2.10 Brass Velocity Gage Electrode Configuration

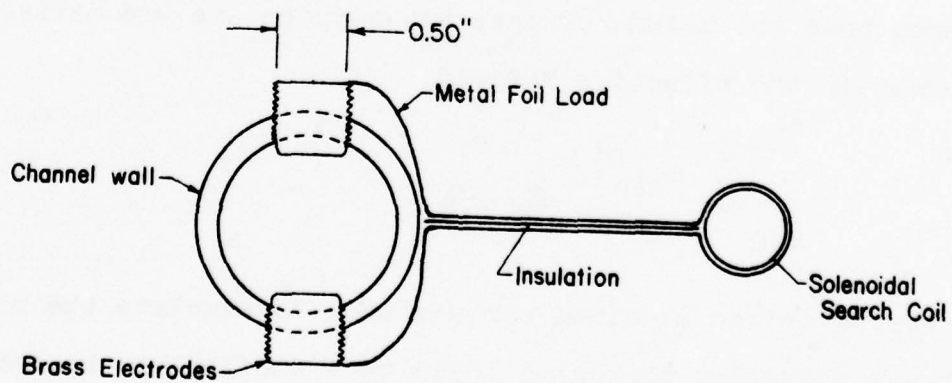


Figure 2.11 End View of Load Circuit Configuration

the field. A lamp and photodiode arrangement was used to measure the bar speed.

The B-field on axis was then measured using a Hall probe, and this center field was compared with the effective field. For the magnet geometry generally used the ratio was found to be

$$\frac{B_{eff}}{B_{center}} = 0.856. \quad (2.7)$$

The center field of each pair of magnets on each shot was measured prior to firing, and the effective field was obtained from this ratio.

2.5.2 Conductivity via Plasma Resistance Measurement

In addition to the velocity gage another Faraday MHD generator was used in the channel to obtain the plasma resistance history and from that the conductivity. In this case the generator is provided with a 10^{-2} ohm resistive load which approximately matches the expected plasma resistance.

The voltage appearing across the load electrodes equals the generator, or open circuit, voltage less the internal voltage drop written as

$$V_L = V_o - iR_i \quad (2.8)$$

where i is the load circuit current and R_i is the plasma, or internal, resistance. The plasma inductive voltage drop, $L \frac{di}{dt}$, is negligible after one or two microseconds. The plasma resistance history can be obtained by measuring V_L , V_o , and i .

The load consisted of a strip of copper or stainless steel foil attached to brass electrodes and folded to make a strip line to minimize the load inductance (≈ 35 nH). Figure 2.11 shows the load circuit arrangement including a search coil inductively coupled to the load to measure the load current. The load voltage is measured across the electrodes, and the open circuit voltage is obtained from the velocity gage record. To do this account must be taken for the time lag between the two diagnostic locations and for differences in B-field amplitude, the load circuit having its own separate pair of barium ferrite magnets.

In order to relate the plasma resistance to the net, or effective, conductivity the gage factor for the particular electrode geometry was measured in the lab using a channel mock-up with copper electrodes and a solution of copper sulfate. To measure the conductivity of the solution the channel section was fitted with copper end plugs. A current was passed through the entire tube, and using the measured current and voltage drop as well as the length and cross-sectional area of the solution the conductivity was found from

$$\sigma = \frac{1}{R} \frac{l}{A} = \frac{1}{V} \frac{l}{A} \quad (2.9)$$

Next a current was passed through the solution via the mock-up electrodes and the resulting current and voltage drop were measured. These electrodes were 0.4 inches in diameter and, like the velocity gage electrodes, protruded 0.1 inch into the channel (see Figure 2.11). Using these measurements and the measured solution conductivity the geometry factor, or gage factor, is found as

$$\Gamma = R \sigma = \frac{V}{I} \sigma \quad (2.10)$$

The plasma conductivity on a shot was then calculated from

$$\sigma(t) = \Gamma / R_1 = \Gamma \frac{1}{V_0 - V_L} \quad (2.11)$$

2.5.3 Conductivity via Eddy Current Measurement

When the plasma flows through a gradient in the B-field, there will likewise be a gradient in the MHD voltage, and this will result in circulating currents in the vicinity of the gradient as illustrated in Figure 2.12. A search coil placed on the outside of the channel will have a voltage induced in it by the variations in the magnetic field

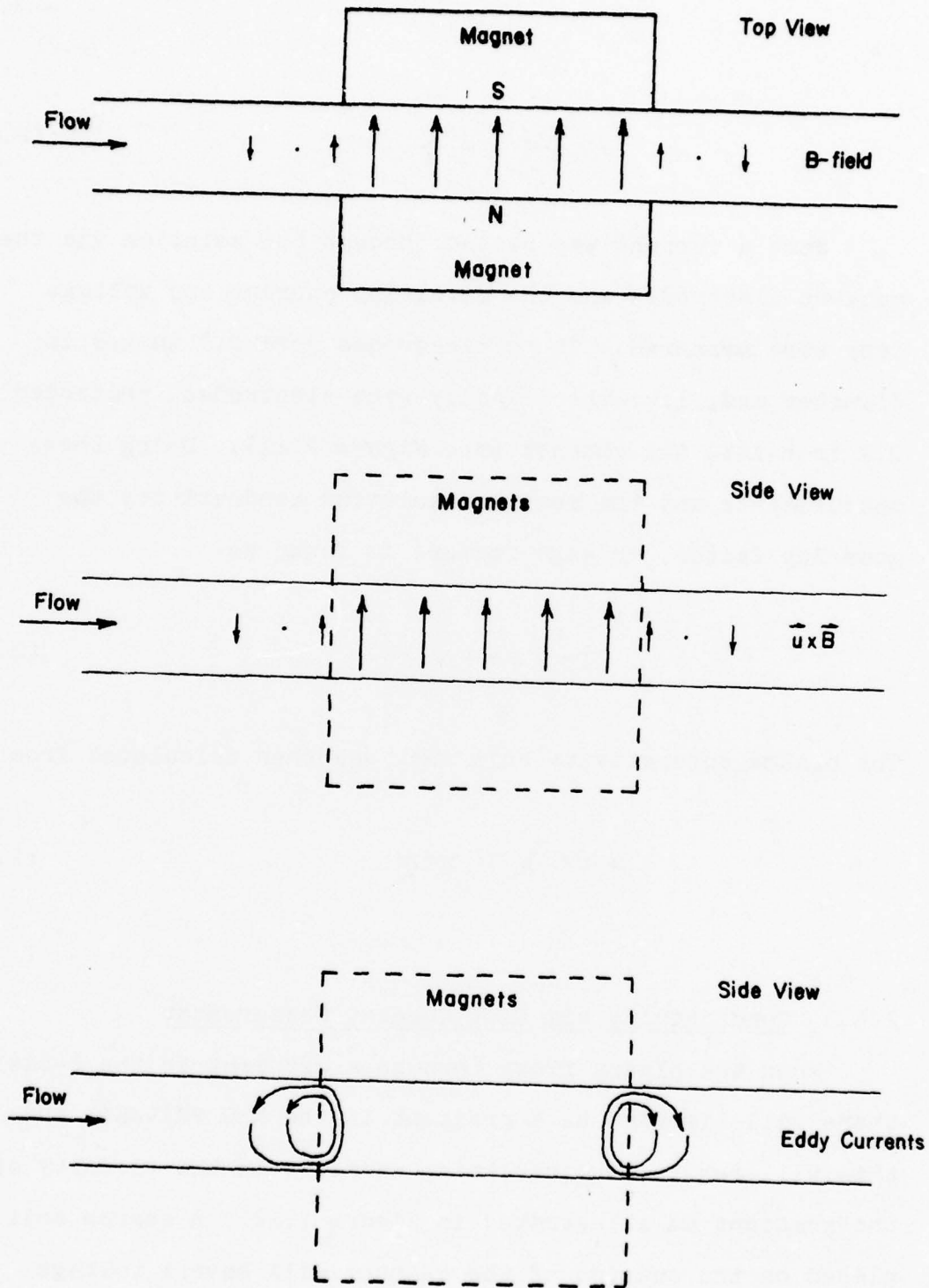


Figure 242 Illustration of Eddy Currents Arising in Plasma Flow Due to Magnetic Field Gradient

produced by the currents.

Output of the search coil is electronically integrated, so that it directly measures the field perturbation caused by the eddy currents:

$$V = \frac{NA\Delta B}{\tau} \quad (2.12)$$

where A is coil area, N is number of turns, and τ is the integrator time constant. The magnetic field perturbation ΔB is a function of magnetic Reynolds number, being theoretically linear with R_m at low values. Thus

$$\Delta B = f(R_m) = f(\mu_0 \sigma u b) \quad (2.13)$$

Calibration of the search coil in the lab is accomplished using the spring gun facility with an aluminum bar simulating the plasma. The magnets and the search coil are first set up in the same geometry as will be used in a shot. Then the bar is propelled through the mock-up at different speeds and the integrated search coil output is measured. From the measured bar speed a plot is made of the search coil output versus bar speed (see the example in Figure 2.13).

Since there are several orders of magnitude difference between the laboratory bar velocities ($u_l \sim 10$ m/sec) and the shot plasma flow velocities ($u_s \sim 10^4$ m/sec), different

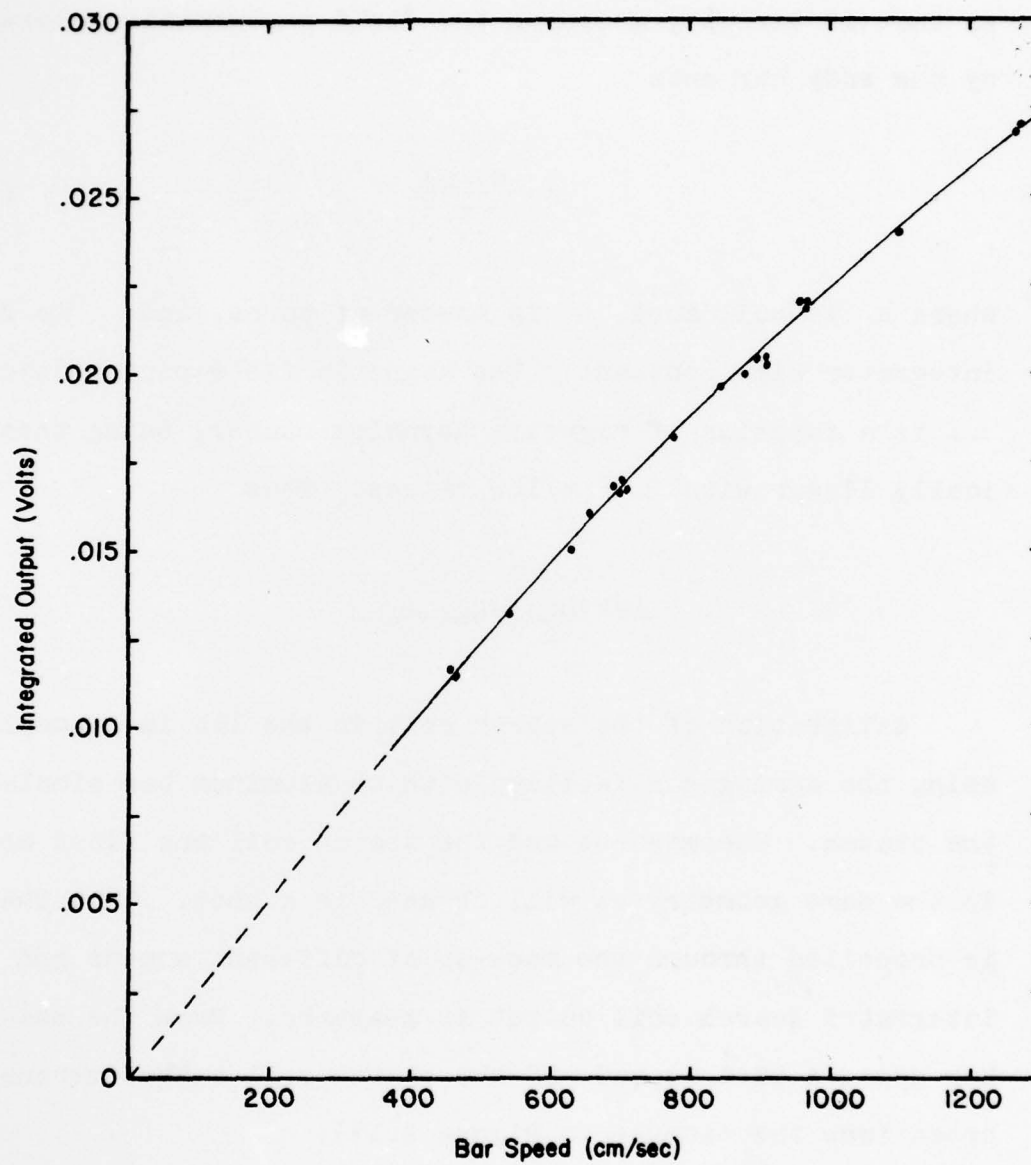


Figure 2.13 Conductivity Gage Laboratory Calibration Curve for Gage No.1, Shot 119-23

time constant integrators are used in the two cases. From the signal level obtained on the shot the corresponding lab bar velocity is obtained from the plot using,

$$u_L = u_L(V_L) \quad (2.14)$$

and

$$V_L \tau_L = V_S \tau_S \quad (2.15)$$

where the L suffixes denote lab parameters and the S suffixes denote shot parameters. The V's are integrated search coil output voltages, and the τ 's are integrator time constants.

Since the same output signal levels (i.e. V_τ) imply the same Reynolds number, or σu , the plasma conductivity is obtained from

$$\sigma_s = \frac{\sigma_L u_L}{u_s} \quad (2.16)$$

The conductivity of the aluminum bar is 2.49×10^5 mho/cm, and the shot flow velocity is obtained from the velocity gage or inferred from the shock speed.

On Shot 119-23 a conductivity gage employing a different field geometry was used in addition to the gages described above. In this case a toroidal barium ferrite magnet was

polarized to give a radially inward B-field which in the plasma channel results in an azimuthal MHD voltages and current flow. The search coil was wound around the channel and was located just beneath the magnet for maximum sensitivity.

The calibration procedure was essentially the same as for the other conductivity gage type. The magnet and coil were set up on the spring gun facility, and the aluminum rod was used to simulate the plasma and thus give integrated search coil output versus bar speed.

2.5.4 Optical Pyrometer

To measure the plasma temperature a small optical pyrometer was developed (using inexpensive parts) which fit onto the diagnostic channel. The geometrical layout of the device is shown in Figure 2.14. The device consists essentially of an aluminum housing, an optical train, and a silicon photo transistor detector. The optical train has a 0.0343 cm diameter pinhole drilled in one-mil stainless steel, a steel apertur, a 90 Å width band-pass optical filter centered at 4500 Å, and several pieces of Pyrex as fillers. In addition on one shot a neutral density filter was added as an attenuator.

The phototransistor type designated MRD 300 was chosen as the detector because of its low cost, relatively high output into 50 ohms ($\sim .1$ volt) and fast response time

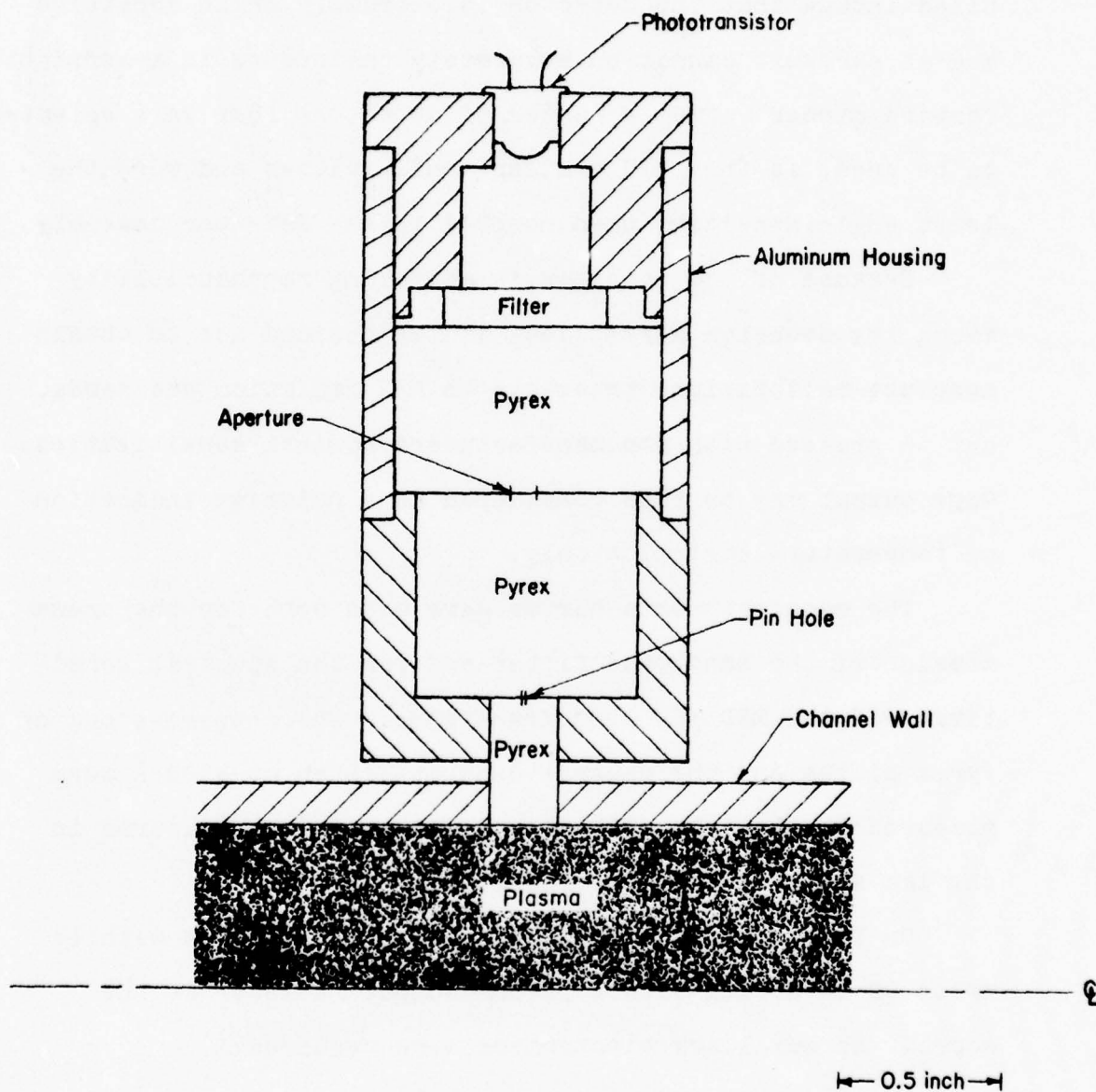


Figure 2.14 Geometrical Layout of Optical Pyrometer

($\approx 1 \mu\text{sec}$). A lens on the front of the detector greatly increases the effective area of the silicon chip, but has the disadvantage that the detector is extremely angle sensitive and as a result cannot be accurately calibrated in a straightforward manner. From a number of detectors four were selected to be used, as they had similar sensitivities and were the least angle sensitive when mounted in the detector assembly.

Because of the problems in achieving reproducibility among the detector assemblies, it was decided not to obtain absolute calibrations traceable to NBS radiation standards, but to proceed with the manufacturers nominal sensitivities. Gage output may be thus considered as a relative indication of temperature variation only.

The manufacturer's curves were used both for the transmission of the band-pass filter and for the spectral sensitivity of the MRD 300 phototransistor. The transmissions of the Pyrex pieces and the neutral density filter at 4500 \AA were measured in the lab. The pinhole diameter was measured in the lab with an optical comparator.

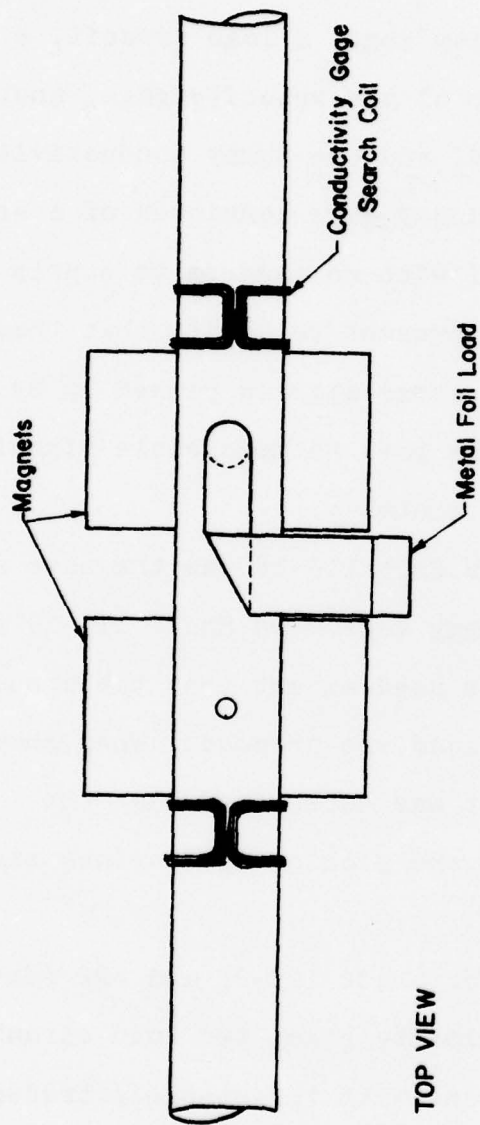
On the shots the phototransistor was provided with 18 volts DC in series with a 50-ohm output resistor at the scope. No auxiliary electronics were required.

2.5.5 Experimental Configurations

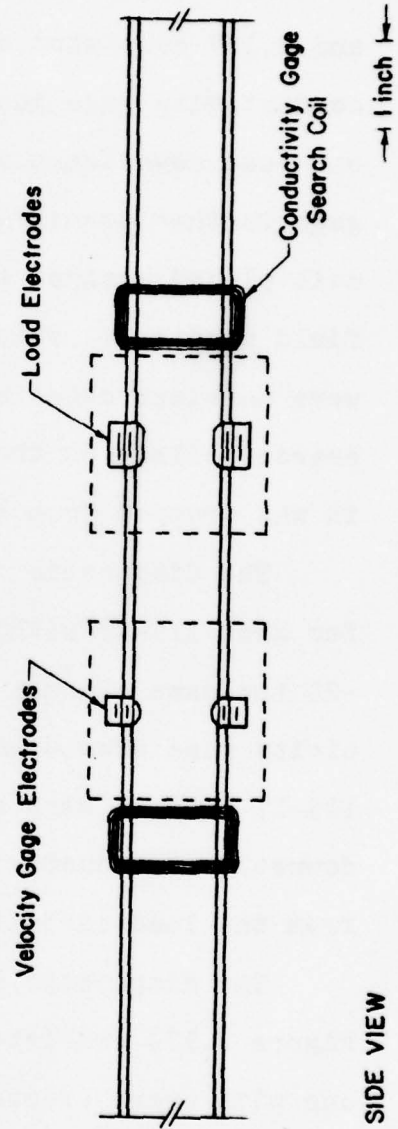
The diagnostic channel for Shot 119-17 (see Figures 2.15 and 2.16) consisted of a velocity gage, a load circuit, a conductivity gage just upstream of the velocity gage, another one just downstream of the load, and one dummy conductivity gage further downstream. The dummy gage consisted of a search coil placed against the channel with no magnets to supply a field gradient. This gage was present to verify that there were no electrostatic or other stray signals picked up by the search coils. As the dummy gage gave no measurable signal, it was dropped from subsequent shots.

The diagnostic channel for Shot 119-18 was the same as for Shot 119-17 without the dummy gage. On Shots 119-19 and -20 the same channel layout was used except that the conductivity gage downstream of the load was dropped. When Shots 119-17 and -18 were analyzed it was determined that the downstream conductivity gages were picking up spurious signals from the load circuit currents.

The diagnostic channels for Shots 119-21 and -22 (see Figure 2.17) consisted of a velocity gage, two load circuits, one with brass electrodes and one with tungsten electrodes, a conductivity gage just downstream of the velocity gage, and an optical pyrometer further downstream. Copper was replaced by stainless steel as the load material.

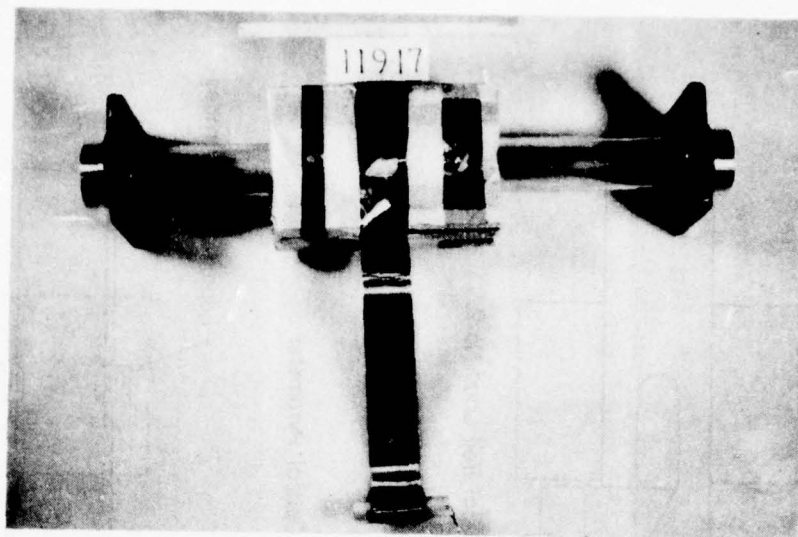


TOP VIEW

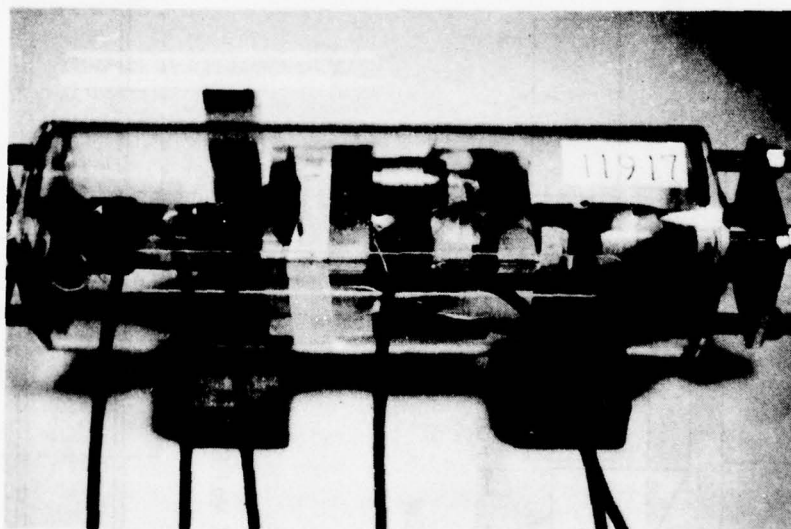


SIDE VIEW

Figure 2.15 Basic Channel Layout for Shots 119-17 thru -20



a) Lexan MHD Channel with Magnets and Copper Foil Load (Shown Unrolled) Attached



b) MHD Channel Mounted in Casting Tube and Ready for Casting

Figure 2.16 Lab Photographs of Typical Diagnostic Channel Assembly

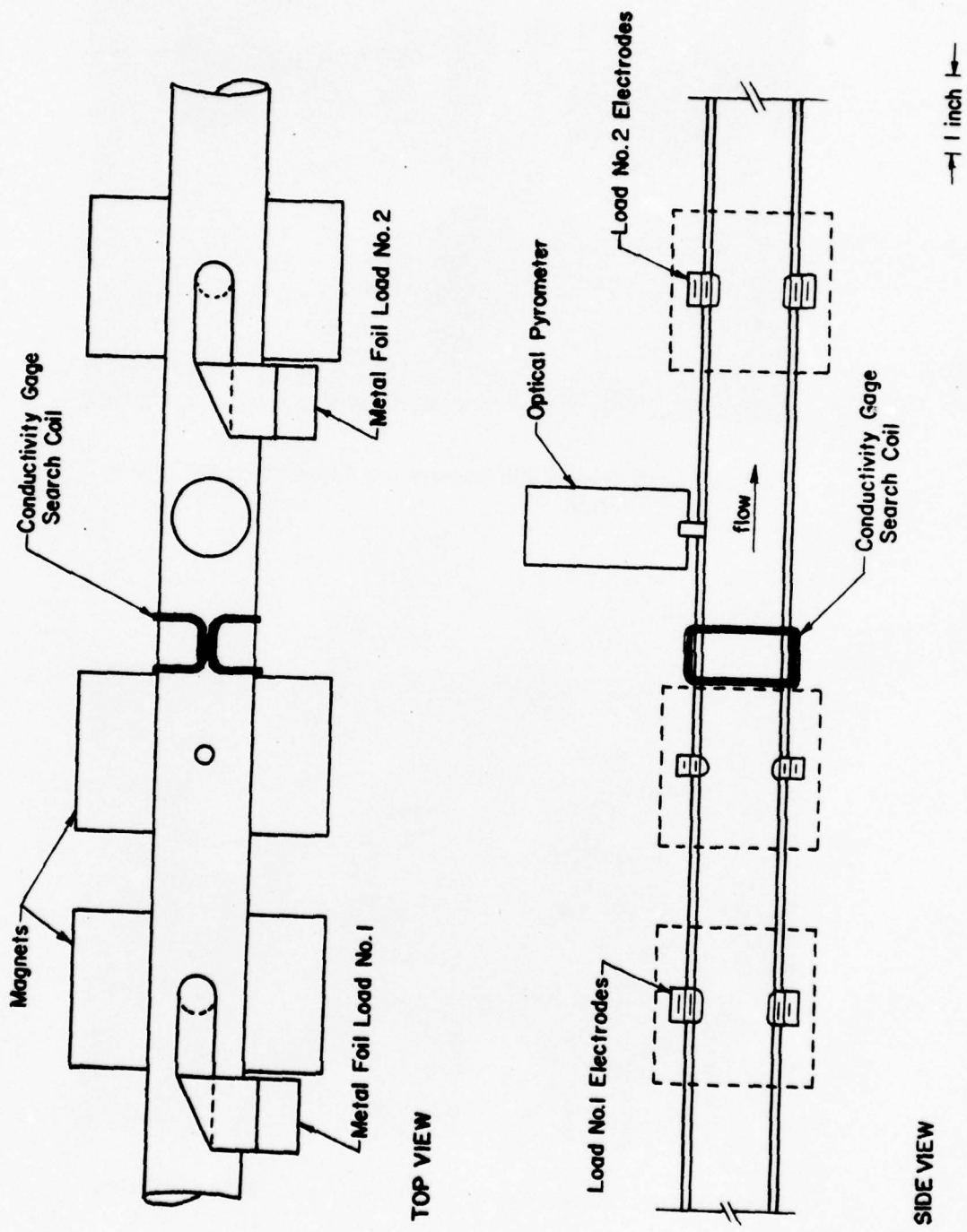


Figure 2.17 Basic Channel Layout for Shots 119-21 and -22

On Shot 119-23 (see Figure 2.18) the load circuits were dropped in favor of adding two additional conductivity gages, one the usual type and the other a toroidal magnet type. The magnets for the velocity gage were removed to the outside of the casting tube and the other square magnets were moved out approximately 2 cm and given neoprene buffers, or shock absorbers. The magnets were moved thus to prevent or delay possible demagnetization by shock waves.

2.6 Experimental Results

2.6.1 Shots 119-17 and 119-18

The results of these two shots are discussed together because of their similarity. They have the same driver type and the same diagnostic design and layout. Experimental oscilloscope traces are shown in Figures 2.19 to 2.22.

The expected flow velocity history at the velocity gage location is a constant $0.85 \text{ cm}/\mu \text{ sec}$ for approximately $15 \mu \text{ sec}$ followed by a decreasing flow velocity. On both shots this corresponds to 16 volts velocity gage output. As can be seen from the traces there are departures from this value of up to 4 volts or 25%, especially in the first $10 \mu \text{ sec}$ of the pulse. Since such variations in the gas flow rate are unlikely, this is probably some spurious signal.

The expected load voltage and current for a constant flow velocity and constant plasma resistance are indicated

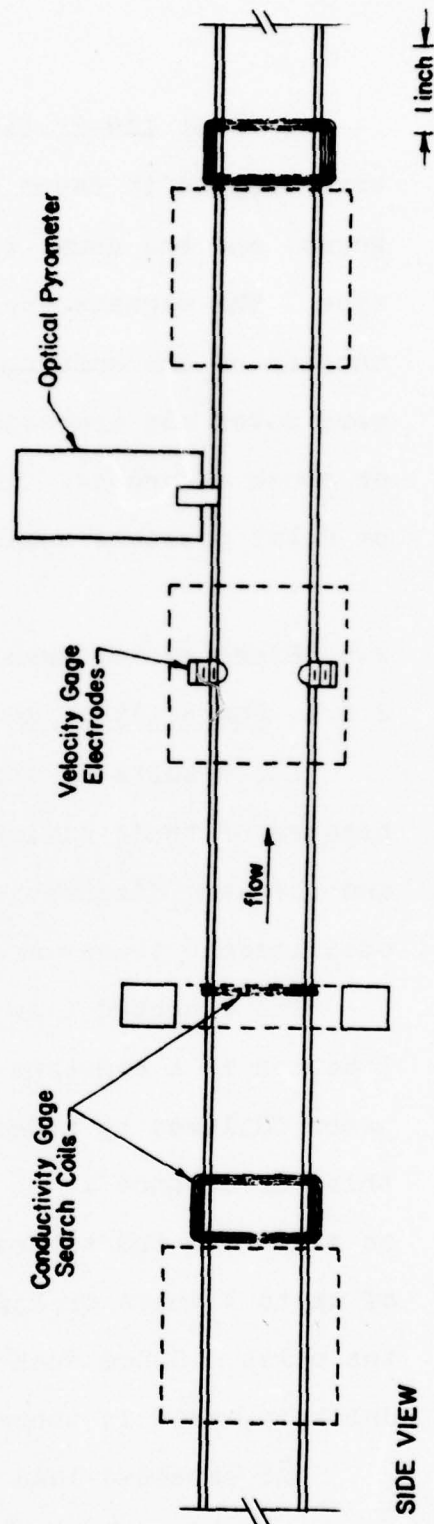
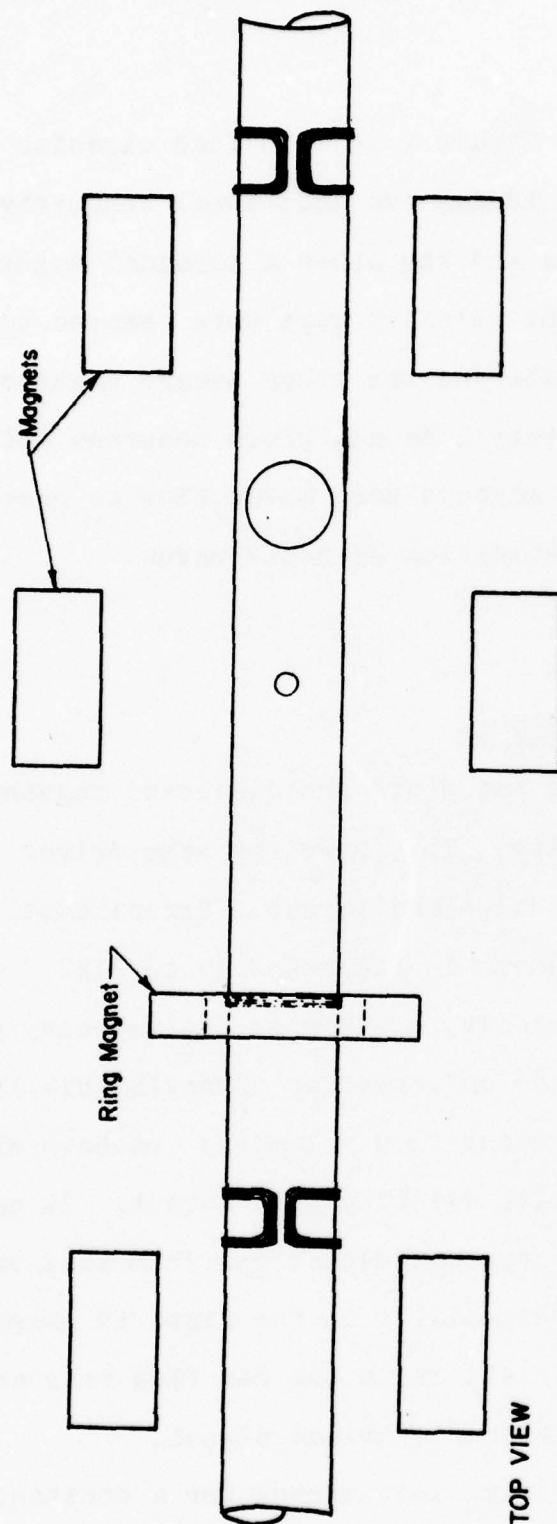
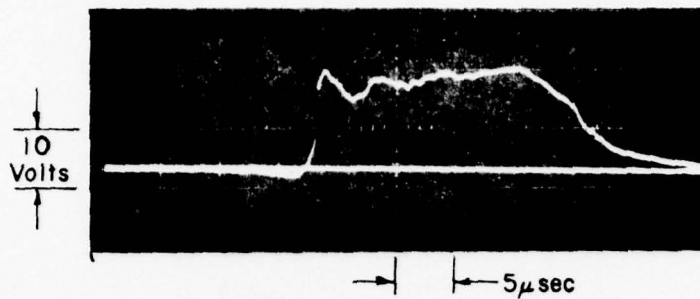
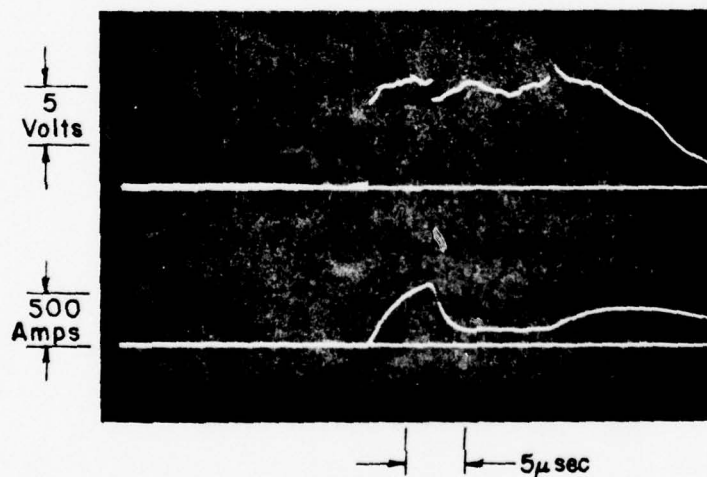


Figure 2.18 Basic Channel Layout for Shot 119-23

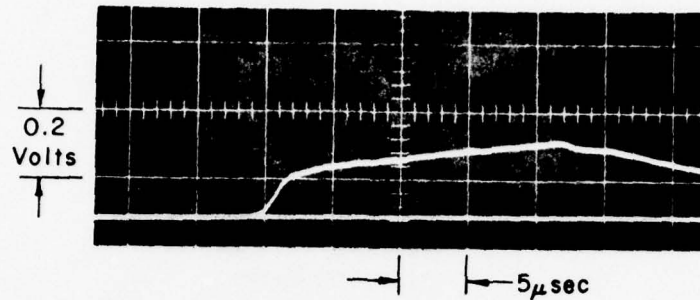


a) Velocity Gage Output Versus Time

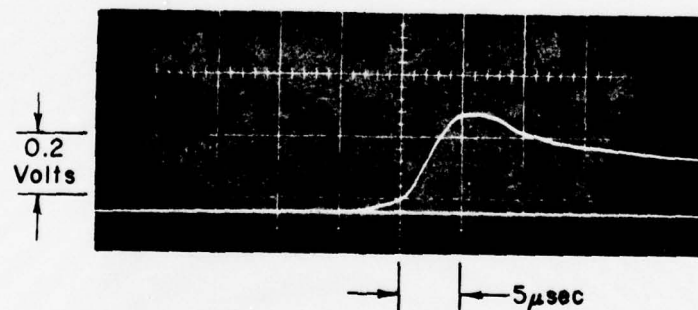


b) Load Voltage (Upper) and Load Current (Lower) Versus Time

Figure 2.19 Velocity Gage and Load Monitor Records for Shot 119-17

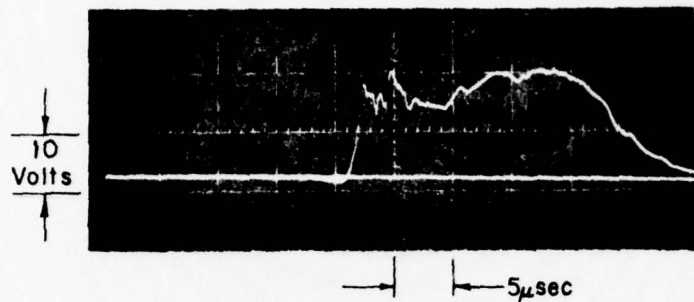


a) Conductivity Gage #1 Output Versus Time

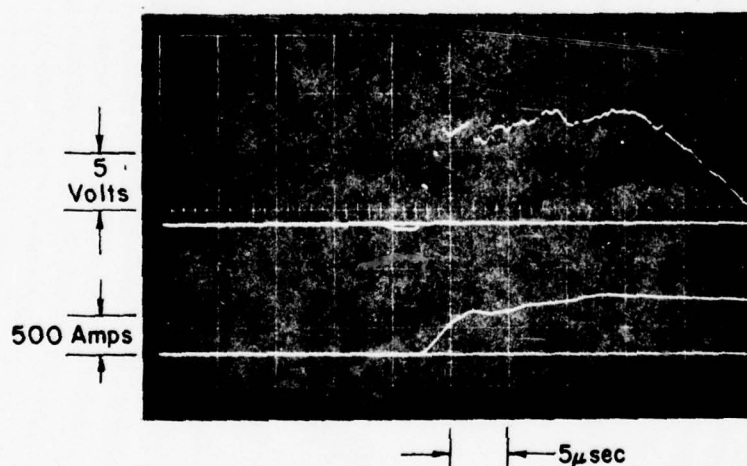


b) Conductivity Gage #2 Output Versus Time

Figure 2.20 Conductivity Gage Records for Shot 119-17

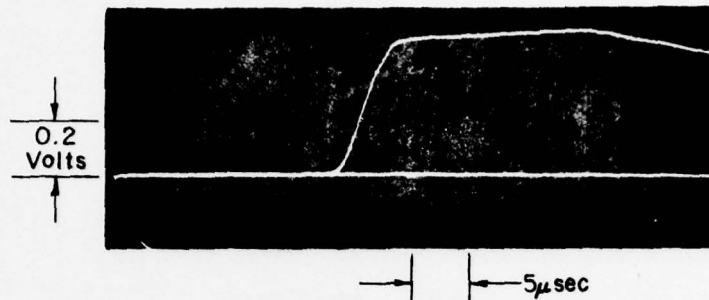


a) Velocity Gage Output Versus Time

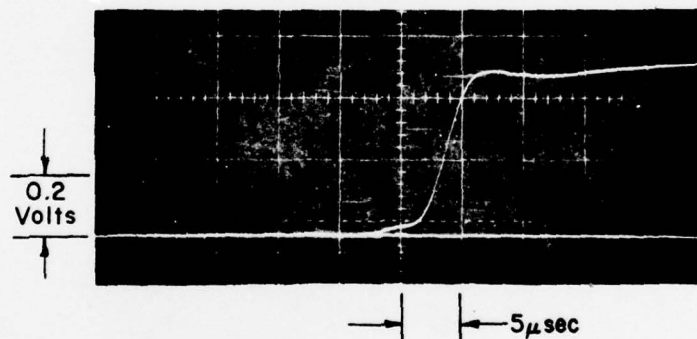


b) Load Voltage (Upper) and Load Current (Lower) Versus Time

Figure 2.21 Velocity Gage and Load Monitor Records for Shot 119-18



a) Conductivity Gage #1 Output Versus Time



b) Conductivity Gage #2 Output Versus Time

Figure 2.22 Conductivity Gage Records for Shot 119-18

in Figure 2.23. V_0 is the generator, or open circuit, voltage, L_i and R_i are the internal inductance and resistance, and L_L and R_L are the external load inductance and resistance.

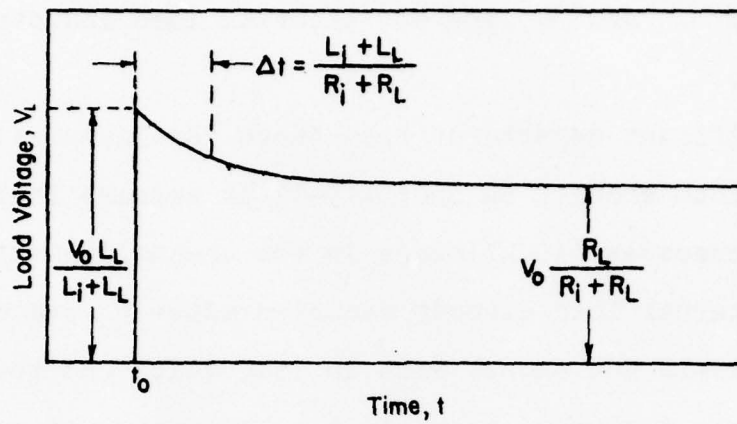
Significant departures from these idealized waveforms occur on both shots. On Shot 119-17 it appears that due to the high stresses (10 kilobars in the channel) partial shorting of the external load circuit occurred after $5 \mu\text{sec}$ of flow. On Shot 119-18 the choppy rise in load volts and the current waveform not returning properly are indicative of problems with the integrity of the load circuit at these high stresses. Nevertheless a value for the plasma conductivity at $5 \mu\text{sec}$ was calculated from these traces using

$$\sigma = \Gamma \frac{i}{V_0 - V_L} \quad (2.17)$$

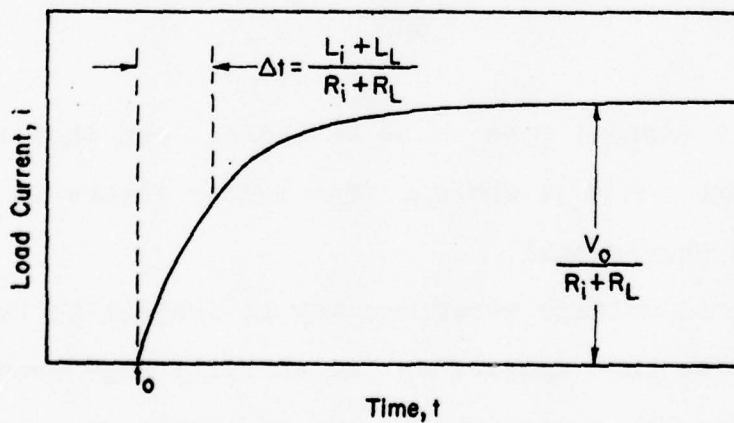
Shot 119-17 (Argon) gave $\sigma \approx 40 \text{ mho/cm}$, and Shot 119-18 (Xenon) gave $\sigma \approx 34 \text{ mho/cm}$. The latter figure is to be considered provisional.

The load voltage waveforms may be subject to the same sort of noise that appears on the velocity gage records, but in this case the variations in the waveforms may also reflect variations in plasma conductivity.

For a constant flow velocity, plasma conductivity, and channel size the conductivity gage outputs should be constant.



a) Load Voltage Versus Time



b) Load Current Versus Time

Figure 2.23 Ideal Load Voltage and Current Waveforms for Constant Flow Velocity and Plasma Resistance

The upstream gages (#1) have a linear rise after the initial startup, while the downstream gages have considerably more structure including a sort of toe or precursor.

The downstream gages are about an inch away from the load electrodes which carried hundreds of amperes on the shots. The precursor part of these conductivity gage signals can be seen to begin simultaneously with the rise of current at the load. No such problems are discernable on the records of the upstream gages which were 4 inches away from the load electrodes. Approximate field calculations support the notion that the downstream gage signals include a component due to current flowing in the load circuit.

Since the conductivity gage outputs are proportional to the channel diameter, it is thought that channel expansion is responsible for the gradual rise in the upstream gage outputs. Using the shock properties of the lead and Hydrostone mixture (assuming that Hydrostone, like grout, has a 5-6% compression at 10 kilobars) the channel expansion rate is found to be 5.5% in 10 μ sec. This does not include consideration of the barium ferrite magnets; nevertheless the increase in the conductivity gage signal from Shot 119-18 is about 5.2% in 10 μ sec. On the other hand the Shot 119-17 data indicates an increase of about 29% in 10 μ sec. It is not clear how the channel could have expanded at that rate unless there were some voids in the casting of lead and

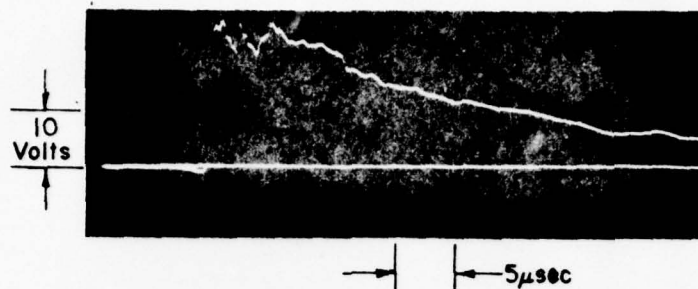
Hydrostone.

Taking the upstream conductivity gage signals at an early time ($5\mu\text{sec}$ after onset) one obtains conductivities of 50 mho/cm for Shot 119-17 and ~ 300 mho/cm for Shot 119-18. The number for Shot 119-18 is only an estimate, since the output on the shot exceeded the range of the original calibration. The estimate was obtained by setting up the same geometry in the spring gun with a different pair of magnets and extending the calibration to higher bar velocities. Since the magnets were slightly different, the calibrations at a given bar velocity are different (e.g. 7% at 700 cm/sec), and therefore the extended calibration is only an approximation to the original.

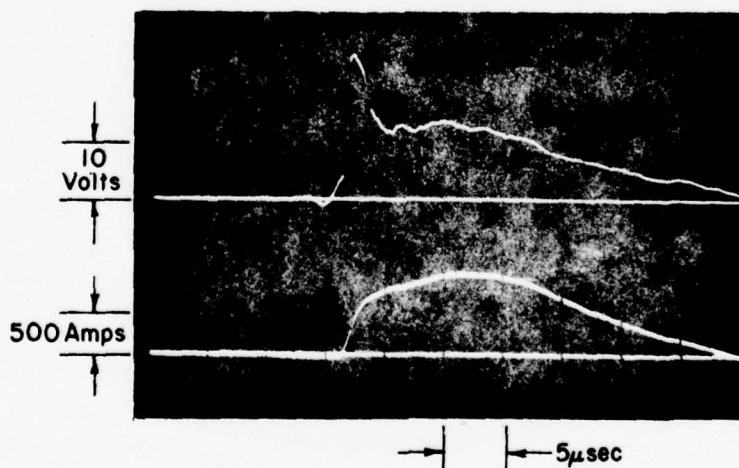
2.6.2 Shots 119-19 and 119-20

These two shots both used disc drivers and identical diagnostic channels. The channels differed from the previous ones only in that the downstream conductivity gage was eliminated.

The data on Shot 119-19 was lost due to early severing of the diagnostic cables by driver debris. A different placement of the cables on Shot 119-20 prevented this problem, and the scope traces are shown in Figures 2.24 and 2.25. The driver gas on this shot was Xenon loaded to give an initial shock pressure of approximately 10 kilobars. The channel gas



a) Velocity Gage Output Versus Time



b) Load Voltage (Upper) and Load Current (Lower) Versus Time

Figure 2.24 Velocity Gage and Load Monitor Records for Shot 119-20

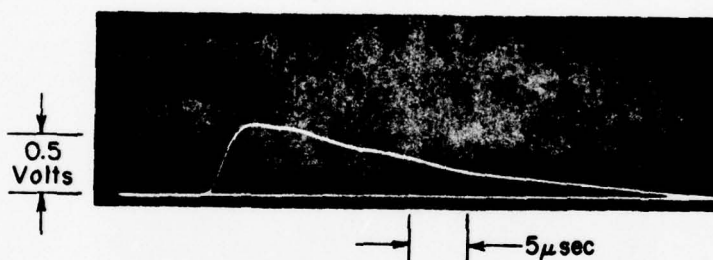


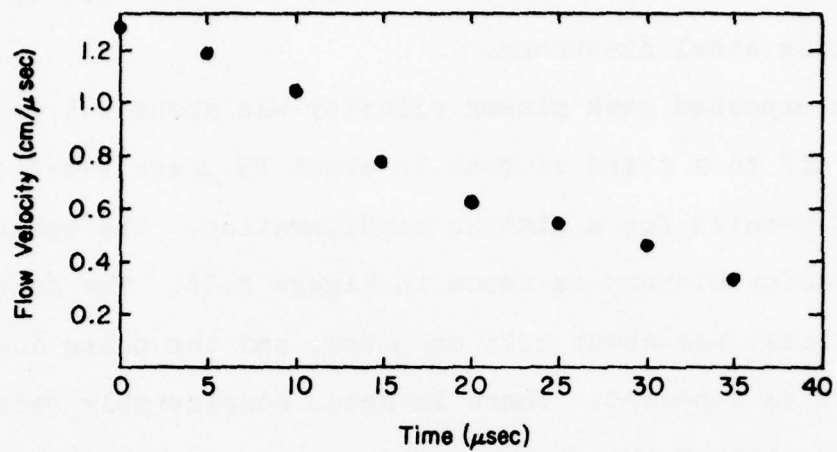
Figure 2.25 Conductivity Gage Output Versus Time for
Shot 119-20

was 1 atmosphere argon separated from the driver gas by a 1-mil-thick steel diaphragm.

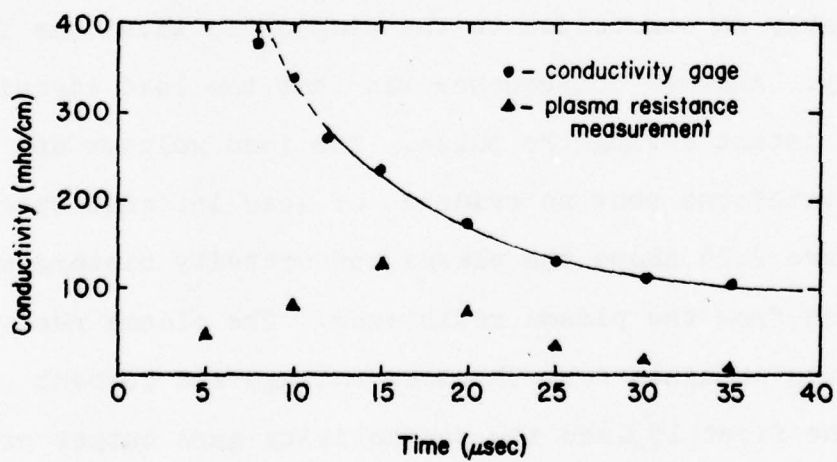
The expected peak plasma velocity was about $1.1 \text{ cm}/\mu \text{ sec}$ falling off to a third of that in about $25 \mu \text{ sec}$ based on previous results for a similar configuration. The measured flow velocity history is shown in Figure 2.26. The initial flow velocity was about $1.25 \text{ cm}/\mu \text{ sec}$, and the pulse duration was about as expected. There is again considerable noise on the early part of the scope record.

Although the pressure history in the channel was not measured, it was a less severe environment than in the previous shots, since the driver gas was expanding into the ambient channel gas. One consequence of this reduced channel pressure is that the channel expansion was significantly less, and probably no correction to the diagnostic waveforms is necessary. Another consequence was that the load circuit survived intact during the pulse. The load voltage and current waveforms show no evidence of load internal breakdown.

Figure 2.26 shows the plasma conductivity history as determined from the plasma resistance. The plasma resistance history was obtained from the load voltage and current records. During the first $15 \mu \text{ sec}$ the conductivity gage output exceeded the range of the calibration. The two earliest time points shown on the graph were obtained by extending the calibration after the shot using a similar pair of magnets on the spring



a) Measured Flow Velocity Versus Time, Shot 119-20



b) Measured Plasma Conductivity Versus Time, Shot 119-20

Figure 2.26 Plots of Experimental Results on Shot 119-20

gun facility. The extended calibration is credible, since the slower bar speed data matched the earlier calibration curve. The point at 8 μ sec is an estimated lower bound, because the output during the first 10 μ sec exceeded the range of the present spring gun configuration.

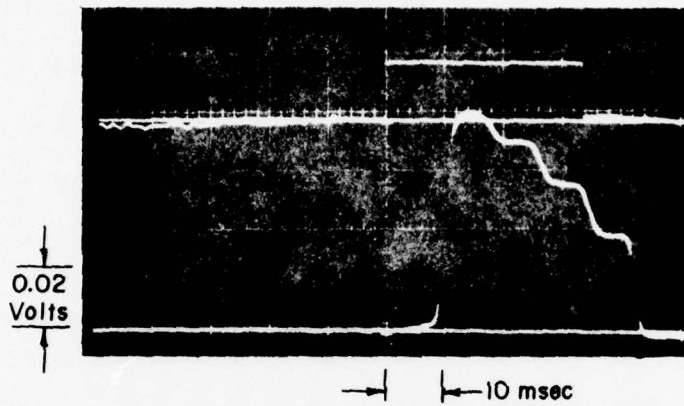
As can be seen in the figure the total interelectrode resistance at the load was decreasing during the first 15 μ sec, and then it increased rapidly after that. Furthermore the apparent conductivity was always considerably lower than the values obtained from the conductivity gage.

Some caution must be exercised in interpreting these, and any other, results of the conductivity measurements. If the plasma conductivity is not uniform across the channel cross-section, it can markedly affect the measurements. Normally there will be a boundary layer on the outer periphery of the plasma whose conductivity is considerably less than that of the main flow. Unless the electrodes are so configured that the electrodes tips protrude through the boundary layer, the total resistance between the electrodes may not at all reflect the conductivity of the main flow. For example, suppose the main flow conductivity was around 300 mho/cm resulting in a plasma resistance of approximately 2 milliohms for our electrode geometry. If there were a 0.01 cm thick boundary layer with conductivity 1 mho/cm over the surface of the 1 cm diameter electrode (or equivalently a

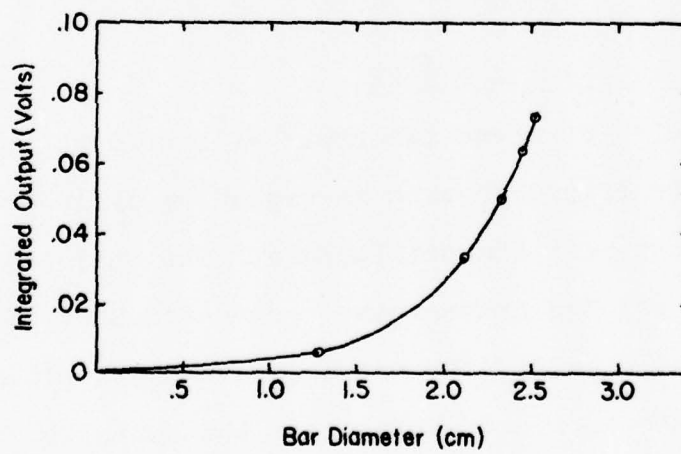
0.1 cm thick layer with 10 mho/cm conductivity), then each electrode surface would contribute 12.7 milliohms to the total resistance. The measured resistance would then be 27.4 milliohms which gives an apparent conductivity of 21.5 mho/cm.

The conductivity gage is also sensitive to variations in the plasma conductivity across the channel cross-section. Since the gage search coil is placed right against the channel wall for maximum sensitivity, and since the pickup is dependent on the coupling between the search coil and the eddy currents in the plasma, a low conductivity boundary layer will result in a significantly reduced output signal.

As an extreme case a stepped bar was shot through the spring gun to simulate a sequence of plasmas with different zero conductivity boundary layer thicknesses. A scope trace for such a test is shown in Figure 2.27, together with a plot of output signal as a function of the bar diameter. A 0.1 cm thick boundary layer of low conductivity will result in a 30% reduction in signal, and, because the output is not linear with Reynolds number, will further reduce apparent conductivity. For example on Shot 119-20 the conductivity gage output at 20 μ sec yielded a plasma conductivity of 177 mho/cm (see Figure 2.26). But if one assumes a 0.1 cm thick boundary layer and a corresponding 30% signal reduction, then working back one finds that the main flow conductivity



a) Conductivity Gage Output Versus Time for a Stepped Aluminum Bar



b) Conductivity Gage Output Versus Bar Diameter

Figure 2.27 Results of Lab Test of Conductivity Gage Response Variations with Bar Diameter

would actually be 300 mho/cm.

Both the plasma resistance measurement and the eddy current field distortion measurement provide spatial averages of the conductivity in the test region. The details of this averaging process are not known at this time, and await the development of a three-dimensional MHD computer code. In the meantime an observation of the governing physical mechanisms indicate that the plasma resistance gage tends to weight the resistive boundary layer heavily, since resistance of adjacent layers is summed. The conductivity gage measures magnetic flux from current flow, and therefore tends to weight the regions of high conductivity. Because of magnetic field divergence considerations, the gage weights current in the core less than current in the boundary layer.

2.6.3 Shots 119-21 and 119-22

The results of these two shots will be described together since they both used an exploding cylinder type driver and identical channel layouts. The only difference between them was the driver gas: argon for Shot 119-21 and xenon for Shot -19-22. The drivers were pressurized to give a 5 kilobar shock, and in both cases the channels were provided with 1 atmosphere of argon separated from the driver by a 1-mil steel diaphragm.

The scope traces are shown in Figures 2.28 - 2.31. The velocity gage records were lost, and after checking out the entire set-up it was tentatively concluded that the problem was an intermittent failure in the oscilloscope. For the purpose of analyzing the data the initial flow velocities were obtained from the measured shock speeds in the channels using the strong shock relation,

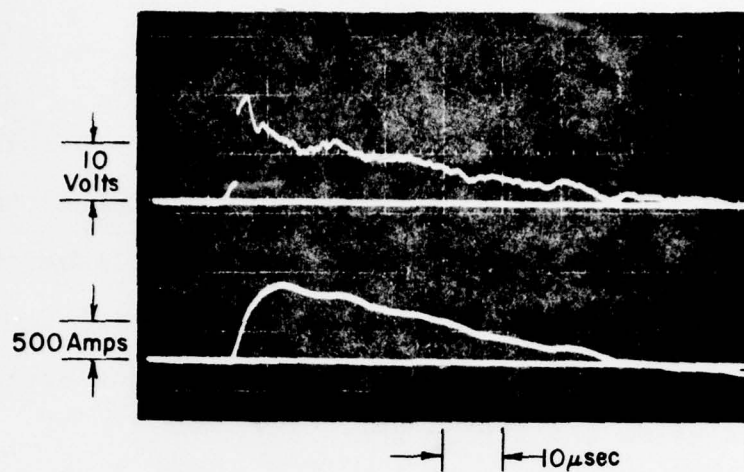
$$U_s = \frac{\gamma+1}{2} u \quad (2.18)$$

where U_s is the shock speed, u is the flow velocity behind the shock, and γ is the ratio of enthalpy to energy. In this case $\gamma = 1.25$, and the data yielded the following:

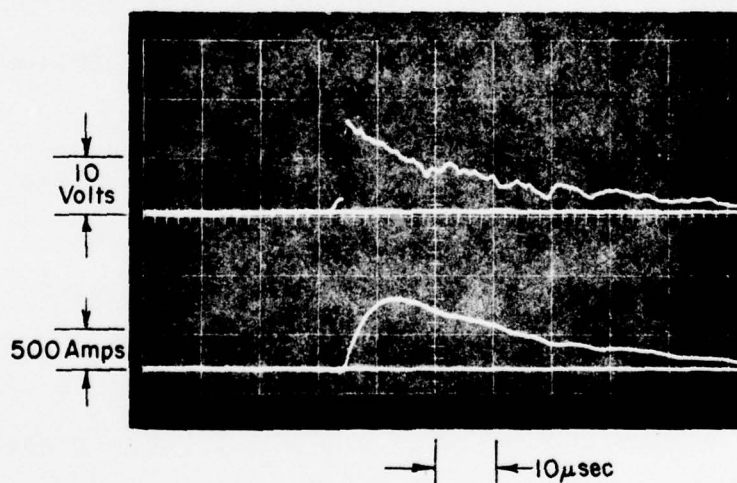
<u>Shot #</u>	<u>U_s (cm/μsec)</u>	<u>u (cm/μsec)</u>	<u>Pressure (kilobars)</u>
119-21	1.070	0.951	1.65
119-22	0.974	0.865	1.36

The channel plasma peak pressures are shown to illustrate that, unlike Shots 119-17 and 119-18, the pressure here is low enough that there is negligible channel expansion or wall motion. Accordingly the load voltage and load current waveforms show no indication of internal load shorting.

The #1, or upstream, loads used brass electrodes of the same shape as on the previous shots, and the #2, or down-



a) Load #1 Voltage (Upper) and Current (Lower)
Versus Time



b) Load #2 Voltage (Upper) and Current (Lower)
Versus Time

Figure 2.25 Load Monitor Records for Shot 119-21

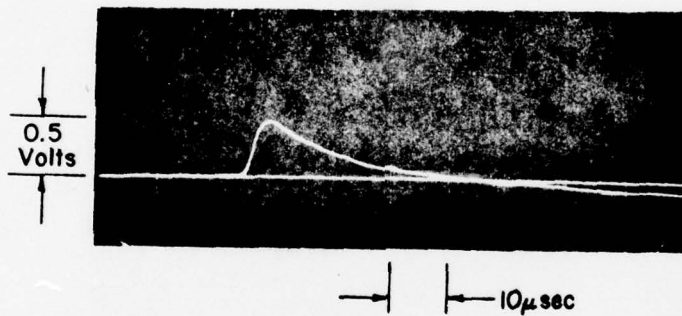
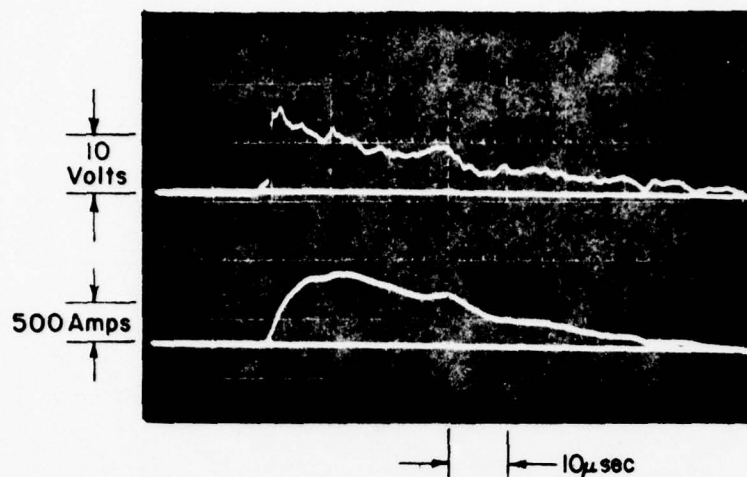
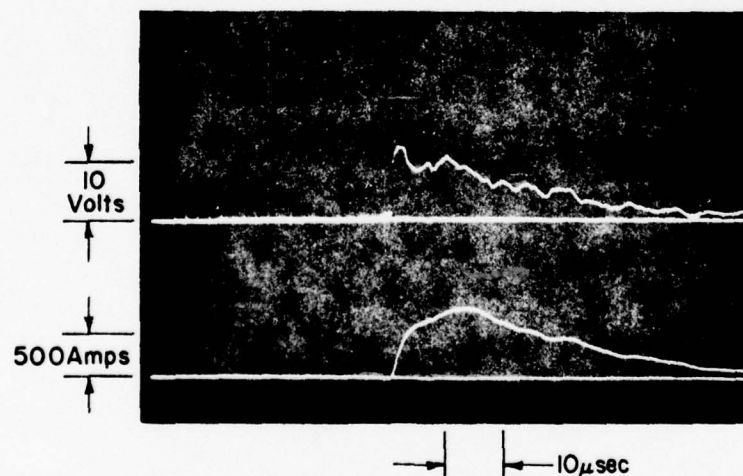


Figure 2.29 Conductivity Gage Output Versus Time for Shot 119-21

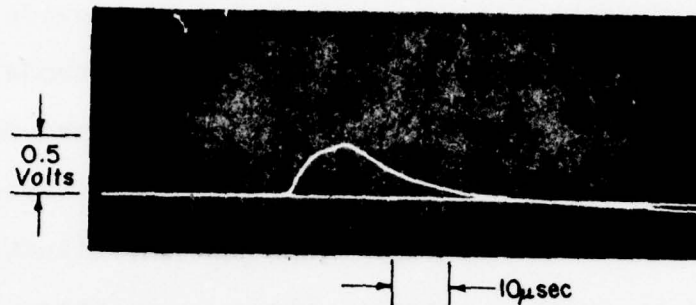


a) Load #1 Voltage (Upper) and Current (Lower)
Versus Time

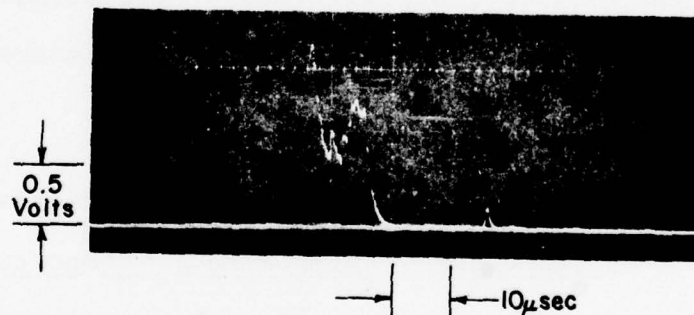


b) Load #2 Voltage (Upper) and Current (Lower)
Versus Time

Figure 2.30 Load Monitor Records for Shot 119-22



a) Conductivity Gage Output Versus Time



b) Optical Pyrometer Phototransistor Output Versus Time

Figure 2.31 Conductivity Gage and Optical Pyrometer Records for Shot 119-22

stream, loads used tungsten tipped electrodes of the same shape. These extra loads were included to provide comparative data on the dependence of the interelectrode resistance on electrode material properties. The argument is that perhaps ablated electrode material itself creates a high resistance boundary layer and that the situation would be improved by using a material whose vapor phase has a higher conductivity.

The initial flow velocities were used to determine the open circuit voltage values for the loads and the flow velocity values for the conductivity gages. Lacking complete velocity histories the conductivities were determined only for 5 μ sec after shock arrival. These results are tabulated below.

<u>Shot #</u>	<u>Load #1 (Brass) (mho/cm)</u>	<u>Load #2 (Tungsten) (mho/cm)</u>	<u>Conductivity Gage (mho/cm)</u>
119-21 (Argon)	98	68	145
119-22 (Xenon)	83	51	119

Since the first approximately 8 μ sec of flow on both shots consisted of compressed argon channel gas and since the driver on Shot 119-22 performed measurably poorer of the two, the conductivities at 5 μ sec would be expected to be lower for Shot 119-22.

Contrary to expectation the tungsten tipped electrodes did not show a higher apparent conductivity than the brass electrodes. That the apparent conductivity was lower may reflect a falloff in conductivity with axial position due to progressive contamination since the tungsten tipped electrodes were 9 inches further downstream than the brass electrodes.

On Shot 119-22 there is a marked increase in load voltage and current at both loads and an increase in conductivity gage output corresponding in each case to the arrival of the xenon driver plasma. The difference between the two shots can be illustrated by comparing conductivities at $10 \mu\text{sec}$ obtained from the conductivity gage outputs and the initial flow velocity. The actual flow velocity may be 5 to 10% lower, so these results are only approximate. At $10 \mu\text{sec}$ the conductivity of the argon driver plasma (Shot 119-21) is approximately 96 mho/cm and the conductivity of the xenon driver plasma (Shot 119-22) is approximately 147 mho/cm.

On Shot 119-21 the optical pyrometer phototransister record was off scale, and so the scope sensitivity was adjusted for Shot 119-22. The scope record is shown in Figure 2.31. The initial peak in the shocked argon channel gas rapidly decays, and this is followed by an increased output upon the arrival of the xenon driver plasma. The rapid fall-off after $10 \mu\text{sec}$ is thought to be due to shock damage to the silicon photo-

transistor. Since the shocked argon should be at a roughly constant temperature, the decaying signal is suggestive of a growing boundary layer obscuring the main flow.

One brass electrode was recovered after each shot. The base of one tungsten-tipped electrode was also recovered, but the tip had been sheared off and was not located. A brass electrode from one of the earlier shots was also recovered at this time. All of these electrodes had a similar ablation pattern which is illustrated in Figure 2.32.

Since there was no ablation observed on the remainder of the surface, it was hypothesized that effective thermal and electrical contact with the plasma may have occurred only on this surface. In the lab sample electrodes were painted and a similar area was filed away to expose the underlying metal. The gage factor for these electrodes was measured and found to be greater than that of the fully exposed electrodes by a factor of 1.7.

If the hypothesis were true, then it would be expected that the gage factor would be higher yet early in the pulse when only a small amount of ablation had occurred. This is consistent with the observed apparent conductivity for the first 15 μ sec on Shot 119-20 (see Figure 2.26). In fact multiplying the apparent conductivity at 15 μ sec by the factor 1.7 gives a value of 218 mho/cm which compares well with the conductivity gage measurement of 236 mho/cm.



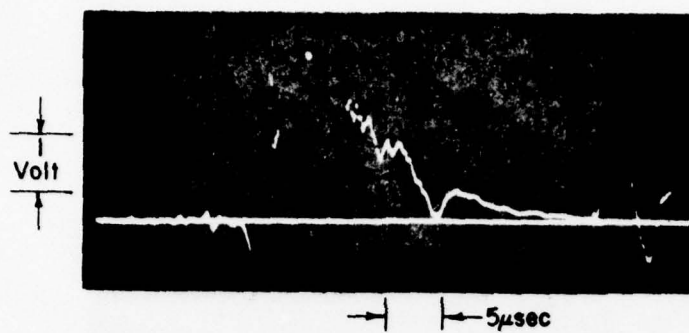
Figure 2.32 Typical Ablation Pattern Observed on Load Electrodes

2.6.4 Shot 119-23

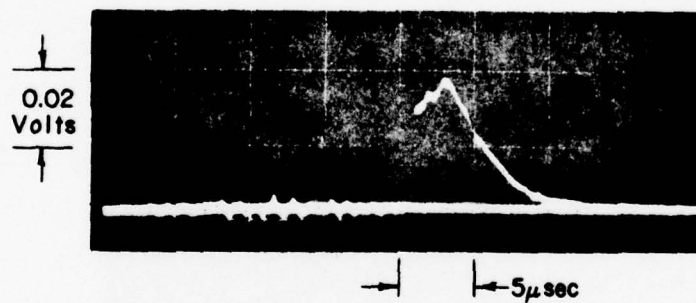
This shot used an imploding cylinder type driver pressurized to give approximately 10 kilobar shock in xenon gas. The channel was merely an inert continuation of the driver pressure tube as in the case of Shots 119-17 and 119-18. That is, there was no diaphragm separating a channel gas at low pressure. The desire here was to repeat the most interesting and straightforward configuration, namely xenon plasma at 10 kilobars pressure and $0.85 \text{ cm}/\mu\text{sec}$ constant flow velocity, and obtain an accurate conductivity measurement. The scope traces are shown in Figures 2.33 and 2.34.

A first attempt was made to eliminate the noise on the velocity gage. The hypothesis was advanced that stress waves in the barium ferrite magnets might result in some amount of demagnetization. Accordingly the magnets were moved to the outside of the tamper reducing the B-field and hence the signal level by a factor of 6 or 7. The magnets for the conductivity gages were moved 2 cm away from the channel wall, and pieces of neoprene were placed in front of them to provide additional shock isolation.

As can be seen on the scope trace (Figure 2.33) the noise level is still several volts while the expected signal amplitude is only 2.5 volts. Fortunately in this case the flow velocity can be obtained from the driver diagnostics. Furthermore it now appears that the source of the noise is

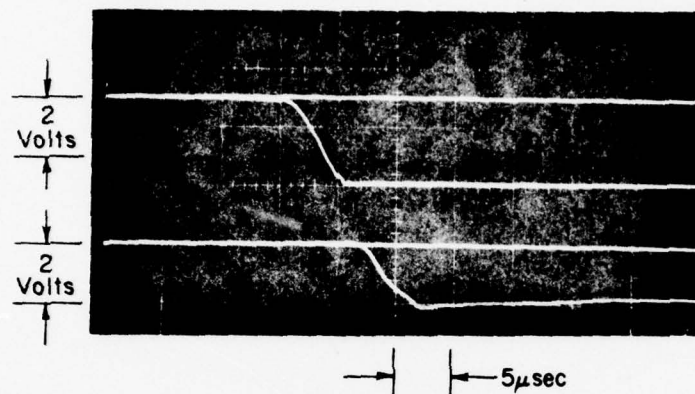


a) Velocity Gage Output Versus Time

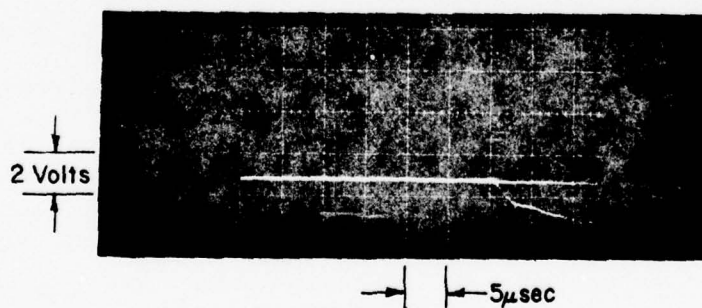


b) Optical Pyrometer Phototransister Output Versus Time

Figure 2.33 Velocity Gage and Optical Pyrometer Records for Shot 119-23



a) Conductivity Gage #1 (Upper) and Conductivity Gage #2 (Lower) Outputs Versus Time



b) Conductivity Gage #3 Output Versus Time

Figure 2.34 Conductivity Gage Records for Shot 119-23

something other than problems with stress waves in the magnets.

Shock waves in dielectric media commonly give rise to transient voltages which, in the case of coaxial cables, result in noisy signals. Since in these experiments coaxial cables extend into the high stress regions, it is possible that such signals are responsible for the noise. However, a careful mock-up of the experimental configuration in the lab using sharp hammer blows on confined sections of coaxial cable gave only sub-millivolt noise levels. To be sure open circuited cable gave responses of several volts, but with the cable end short-circuited to simulate the channel plasma no appreciable signals were observed.

Because the magnets on the conductivity gages were moved away from the channel, the B-field gradient was significantly reduced. In order to get reasonable amplitude signals (> 0.1 volts) it was necessary to switch from passive R-C integrators to operational amplifier driven integrators, particularly for conductivity gage #2 with its radially polarized ring magnet.

Although the integrators were carefully calibrated and checked-out in the lab, apparently some DC shift at the test-site instrumentation bunker resulted in the outputs topping out at 2-3 volts. As a result the first two conductivity gages did not give a complete record (see Figure

2.34(a)). From the peak recorded outputs the lower bounds on the conductivity are 340 mho/cm at conductivity gage #1 and 284 mho/cm at conductivity gage #2.

The downstream, or #3, conductivity gage did not top out probably because the signal never exceeded 2 volts anyway. The conductivity measured at 5 μ sec from shock arrival was 130 mho/cm. Subsequent wall expansion and flow velocity changes preclude getting accurate measurements at later times.

In order to bring the phototransistor output of the optical pyrometer down to the linear response range a neutral density filter was included in the detector optical train for this shot. The response as shown in Figure 2.33(b) is more or less flat for approximately 3 μ sec and then rapidly decays. The onset of decay corresponds to the expected arrival of the release wave from the driver piston. The peak output is 32 millivolts which corresponds to a temperature of 4.3 eV based on the estimated response curve. The predicted temperature for this xenon plasma at 10 kilobars is 4.4 eV.

2.6.5 Summary of Conductivity Measurements

The results of the conductivity measurements are presented together in Table 2.3. The table gives the results for each shot showing the type of driver, the gas used, and the initial plasma flow velocity. The results from the conductivity gages

TABLE 2.3
SUMMARY OF CONDUCTIVITY MEASUREMENTS*

Shot No.	Driver Type	Driver Gas	Channel Flow Velocity (cm/ μ sec)	Conductivity via Conductivity Gage (mho/cm)	Conductivity via Plasma Resistance (mho/cm)	Axial Location of Probe (cm)	Comments
119-17	Imploding Cylinder	Argon	0.85	50	40	10.2 20.3	
119-18	Imploding Cylinder	Xenon	0.85	~ 300	~ 34	12.7 22.9	
119-20	Disc	Xenon	1.25	> 400	47	12.7 22.9	
119-21	Exploding Cylinder	Argon	0.95	145 96	98 68	25.4 25.4 15.2 38	Argon Channel Gas Argon Driver Gas, 10 μ s Brass Electrodes Tungsten Electrodes
119-22	Exploding Cylinder	Xenon	0.86	119 147		25.4 25.4 15.2 38	Data for Argon Channel Gas Xenon Driver Gas, 10 μ s Brass Electrodes Tungsten Electrodes
119-23	Imploding Cylinder	Xenon	0.85	> 340 > 284 130	83 51	11.4 19.0 41.9	

*All measurements at 5 μ sec from shock arrival except where noted.

and the conductivities determined from plasma resistance measurements are shown in separate columns. Since there appears to be some dependence on the axial location of the detector, the distance of the detector from the beginning of the Lexan channel is also shown for each measurement.

In most cases conductivity measurements could only be accurately made in the early part of the pulse. Accordingly the conductivities shown in the table refer to a measurement at 5 μ sec after shock arrival except where noted.

The most striking feature of the data is the consistently lower apparent conductivities obtained by plasma resistance measurements. Some of the data supports the hypothesis that good electrical contact with the plasma is made over a small portion of the electrode surface actually being ablated by the flow. Then in terms of conductivity measurement if the true time-dependent gage factor were known and applied to the measured resistance, the conductivity measurements should agree.

Even if the hypothesis is true, there remains the practical problem of designing electrodes which are in good electrical contact with the plasma over their entire surface. There is not enough difference in apparent conductivity between the brass and tungsten electrodes on Shots 119-21 and 119-22 to support the notion that the problem is material specific. Furthermore previous measurements (Ref-

erence 1.2) using various electrode shapes including wedge-shaped and finned, or slotted, electrodes likewise gave apparent conductivities in the 40-100 mho/cm range. Therefore it is not clear that modifying the electrode shape will significantly alter the performance.

It was generally observed that xenon gave higher conductivities than argon for similar conditions. Different types of drivers likewise gave significantly different conductivities. Since the thermodynamic conditions were different in each case, however, the results could not be correlated as to driver contamination. In the theoretical work it was found that for these plasma conditions the conductivity is a sensitive function of the thermodynamic conditions. Therefore the question of driver plasma contamination will have to be deferred until each of the measured conductivities can be compared with theoretical values at the appropriate thermodynamic conditions.

3. THEORETICAL PROGRAM

3.1 Purpose

The ability to make reliable predictions of the equilibrium thermodynamic properties of explosively driven plasmas is needed for realistic experimental design and for optimization studies. In the case of self-excited MHD power sources, it is necessary to go one step further and develop methods for determining the electrical conductivity of the plasma.

The purpose of the theoretical program was to review the state of the art of predictive methods for explosively driven plasmas, to perform preliminary calculations as an aid to identifying plasma parameter regimes, and to recommend methods for reducing the existing discrepancy between experiment and theory.

3.2 Ideal Plasma Calculations

The standard approach in calculating equilibrium plasma thermodynamic state is based on the assumption of a mixture of ideal gases. This assumption presumes that particle number densities are low enough and temperatures high enough that the average interparticle interaction energy is much smaller than the random (thermal) kinetic energy. For strongly ionized plasma, $\bar{z}^2 e^2 / n_e^{-1/3}$ is a measure of the average electrostatic interaction energy of the charged particles and thus the ideal gas assumption implies that $\gamma \ll 1$ where

Interaction Parameter

$$\gamma = \bar{z}^2 e^2 n_c^h / k T \quad (3.1)$$

In Equation 3.1, \bar{z}^2 is the mean square charge and n_c is the total charged particle number density, i.e.:

$$n_c = n_e + \sum_i n_i \quad (3.2)$$

$$\bar{z}^2 = (n_e + \sum_i z_i^2 n_i) / n_c \quad (3.3)$$

Standard methods for computing the equilibrium thermodynamics of mixtures of ideal gases are based on solving a set of "Saha" equations together with charge and nuclei conservation equations and are fully discussed in several textbooks (e.g. Reference 3.1). One source of ambiguity in this procedure occurs in computing the electronic partition function, given by,

$$Q_{el} = \sum_{j=0}^{\infty} g_j e^{-\epsilon_j / k T} \quad (3.4)$$

where one has to devise some system of truncating the summation with respect to energy levels ϵ_j (g_j is the level degeneracy) in order to avoid the physically unrealistic

infinite sum represented by Equation 3.4.

We have carried out an ideal-gas calculation for a xenon plasma at 10 kbar total pressure and 3.6×10^{11} erg/gm internal energy (corresponding to a shock wave with flow velocity of 8.5 km/sec). In computing these properties we assumed that only the ground state contributes to the electronic partition function sum in Equation 3.4, as most of the truncation schemes drastically curtail the number of contributing energy levels at explosive driver conditions.

Results of our calculations using the ideal gas approximation are shown in Table 3.1. The method fails a self-consistency check, since the calculated value of the interaction parameter γ is 0.57, well outside the range of applicability of the theory.

3.3 Debye-Huckel Calculations

The Debye-Huckel theory (References 3.1 to 3.3) has been widely used in computing thermodynamic properties of weakly nonideal plasmas, and is the logical next step in our approach. This method is based on an approximate evaluation of the screening effect of the surrounding charges on the potential of a given ion according to classical electrostatics and Boltzmann statistics.

The screening length scale or Debye length of the plasma is defined by

TABLE 3.1
RESULTS OF PLASMA CALCULATIONS FOR 10 KBAR
XENON DRIVER CONDITIONS

	<u>Ideal Plasma Approximation</u>	<u>Debye-Huckel without Ion Shielding</u>
Total Pressure (kbar)	10.0	10.0
Internal Energy (erg/g)	3.60×10^{11}	3.60×10^{11}
Density (g/cm ³)	.098	.116
Temperature (eV)	5.07	4.37
Electron Density (cm ⁻³)	7.81×10^{20}	1.01×10^{21}
Total Ion Density (cm ⁻³)	4.48×10^{20}	5.28×10^{20}
Mean Square Charge \bar{Z}^2	1.86	2.06
Atom Concentration (cm ⁻³)		
Xe	2.90×10^{18}	3.45×10^{18}
Xe ⁺	1.40×10^{20}	1.43×10^{20}
Xe ⁺⁺	2.84×10^{20}	2.94×10^{20}
Xe ⁺⁺⁺	2.31×10^{19}	8.79×10^{19}
Xe ⁺⁺⁺⁺	1.06×10^{18}	2.94×10^{18}
Interaction Parameter γ	.565	.783

$$D_c = \left[kT / 4\pi e^2 (n_e + \sum_i z_i^2 n_i) \right]^{1/2} \quad (3.5)$$

Electrostatic interactions led to a lowering of the ionization potential given, for an ion of charge z_i , by

$$\Delta I_{z_i} = (z_i + 1) e^2 / D_c \quad (3.6)$$

and a reduction of the total pressure

$$\Delta P = e^2 (n_e + \sum_i z_i^2 n_i) / 6 D_c \quad (3.7)$$

Thus in solving for the thermodynamic state using the Debye-Huckel procedure, one essentially repeats the steps taken in the ideal gas approximation approach but with new ionization potentials $I_{z_i}^{D-H} = I_{z_i} - \Delta I_{z_i}$ and $p^{D-H} = p^{ideal} - \Delta P$. In calculating the electronic partition functions, one computes the sum in Equation 3.4 to $\epsilon_l \leq I_{z_i}^{D-H}$, thus removing the ambiguities associated with the truncation of the infinite sum.

In attempting to calculate the thermodynamic properties of a xenon plasma with 10 kbar total pressure and 3.61×10^{11} ergs/gm internal energy, we encountered thermodynamic instabilities (characterized by calculated total pressures becoming negative). Since the question of full participation

by the ions in the dynamic coulomb shielding of a plasma is subject to some controversy (Reference 3.34), we decided to try the Debye-Huckel calculations assuming screening by electrons only ie, with the Debye length taken as

$$D_e = [kT/4\pi e^2 n_e]^{1/2} \quad (3.8)$$

This approach leads to thermodynamically stable results which are also shown in Table 3.1.

The question of ion participation in the electrostatic shielding was considered by Devoto (Reference 3.34) who computed electrical and thermal conductivities of argon at 1 atm pressure by solving the Boltzmann collision term with the shielded coulomb potential using both definitions of the Debye length. Comparisons with calculations of Williams and Dewitt (Reference 3.28), who used a quantum mechanical formulation in which the dynamic shielding process was treated correctly, revealed better agreement if shielding by ions was ignored.

The Debye-Huckel technique is generally expected to be valid for high temperatures and low densities (i.e. a weakly nonideal gas) or, equivalently, in the limit that the Debye sphere contains a large number of charged particles. A less restrictive condition for its applicability has been derived (Reference 3.2) from a classical statistical mechanical

study of weak electrolyte solutions. This condition can be expressed in the form,

$$n_c \equiv n_e + \sum_i n_i \geq (8\pi D_c^3)^{-1} \quad (3.9a)$$

or, equivalently,

$$N_{D_c} \equiv \frac{4\pi}{3} D_c^3 (n_e + \sum_i n_i) \geq \frac{1}{6} \quad (3.9b)$$

$$\gamma \leq \pi^{-2/3} = 0.47 \quad (3.9c)$$

This restriction implies that on the average it is necessary to have at least one-sixth of a charged particle in the Debye sphere for the Debye-Huckel theory to be valid. It needs to be pointed out, however, that both the Debye-Huckel theory and the condition 3.9a, b, c for its applicability are based on the assumption of a classical mechanical description of charged particle interaction. As discussed in later sections, quantum mechanical effects play an important role in a strongly nonideal gas and clearly the "real" region of applicability of the Debye-Huckel theory is reduced to values of γ where quantum mechanical effects begin to become appreciable.

Using the Debye-Huckel theory with electronic participation in the shielding process, the thermodynamic parameters of Table 3.1 were calculated. The number of electrons in a Debye sphere is about 0.5, which is within the range of applicability of the theory. The interaction parameter γ is equal to 0.79, indicating a strongly nonideal plasma.

The Debye-Huckel expression has been shown to be the first order term in a perturbation solution of the classical statistical mechanical formulation for nonideal plasmas (Reference 3.2) and much work has been done to evaluate higher order terms (see for example, Reference 3.39). However, this approach is not useful for the strongly nonideal plasmas of interest to us since any improvement on the Debye-Huckel approach must take account of the quantum mechanical effects.

The quantum mechanical effects can be generally subdivided into two types: electron degeneracy effects, and effects associated with the quantum-mechanical phenomena associated with strong (i.e. short-range) charged particle collisions. One approach, widely used in reentry physics and nuclear fireball calculations about a decade ago, is based on the ion-sphere theory of plasma interaction. In this approach, one accounts for electron quantum degeneracy effects by treating the electrons within the framework of a finite temperature Thomas-Fermi statistical model. In

fact a general theory (Reference 3.6) is available which provides the Debye-Huckel and the ion-sphere solutions as limiting cases (high temperature, low density limit for the former and low temperature, high density limit for the latter). However, this approach is inadequate for plasma conditions of interest to us where it is essential to account for quantum mechanical collision effects. Indeed the breakdown of thermodynamic stability associated with a Debye-Huckel theory based on full ion participation in the screening process is an indication of the need to account for the quantum collisional effects.

3.4 Parameters Characterizing Plasma Regime

It is useful at this stage to consider the parameters that characterize the plasma regime. We consider a multiply ionized plasma for which $n_c = n_e + \sum_i n_i$ is the total charged particle number density and $\bar{Z}^2 = (n_e + \sum_i Z_i^2 n_i) / n_c$ is the mean square charge on a charged particle. There are five primary length scales as follows:

Debye length:

$$D_c = (kT / 4\pi \bar{Z}^2 e^2 n_c)^{1/2} = 7.343 \times 10^{10} (T / \bar{Z}^2 n_c)^{1/2} (\text{\AA}) \quad (3.10)$$

Average Impact Parameter:

$$\bar{b}_0 = \bar{Z}^2 e^2 / 3 k T = 4.800 \bar{Z}^2 / T (\text{\AA}) \quad (3.11)$$

Thermal DeBroglie Wavelength of Electrons:

$$\lambda_e = \hbar / (2 m_e k T)^{1/2} = 1.952 / T^{1/2} (\text{\AA}) \quad (3.12)$$

Average Charged Particle Separation

$$r_c = n_e^{-1/3} \quad (3.13)$$

Average Electron Separation

$$r_e = n_e^{-1/3} \quad (3.14)$$

The Debye length is a measure of the effective range of the coulomb potential. As mentioned in the previous section, it can be defined in terms of electron participation in the shielding process ($D=D_e$) or participation by both electrons and ions ($D=D_c$). \bar{b}_0 is the average classical impact parameter for 90° scattering and qualitatively delineates strong and weak scattering regions.

From these primary length scales we construct the following important dimensionless parameters with which we can characterize

the plasma regime.

Interaction Parameter:

$$\gamma = \bar{z}^2 e^2 n_c^{1/2} / kT = 1.440 \times 10^{-7} \bar{z}^2 n_c^{1/2} / T \quad (3.15)$$

Plasma Parameter

$$\Lambda_c = D_c / b_0 = \frac{3}{2\pi^{1/2}} \cdot (T / \bar{z}^2 e^2)^{3/2} / n_c^{1/2} = \frac{3}{2\pi^{1/2}} \gamma^{-1/2} \quad (3.16)$$

Number of particles in Debye Sphere

$$N_{D_c} = \frac{4\pi}{3} D_c^3 n_c = \Lambda_c / g = \frac{1}{6\pi^{1/2}} \gamma^{-3/2} \quad (3.17)$$

Quantum Diffraction Parameter

$$\lambda_e / D_c \quad (3.18)$$

Electron Degeneracy Parameter

$$\lambda_e / r_e \quad (3.19)$$

A classical nonideal plasma is completely characterized by the interaction parameter γ . Both the plasma parameter Λ and the number of charged particles in the Debye sphere, N_D can be expressed in terms of it. The importance of

quantum mechanical effects is characterized by two additional parameters, λ_e/r_e representing electron degeneracy effects, and the quantum diffraction parameter λ_e/D which characterizes the quantum nature of the collisional interaction of electrons with other electrons or ions. It is useful to note that, in the weakly nonideal plasma limit, the five primary length scales are ordered according to:

$$\lambda_e \ll \bar{b}_0 \ll (r_e, r_c) \ll D_c \quad (3.20)$$

and hence in this regime ($\gamma \ll 1$, λ_e/D_c , $\lambda_e/r_e \ll 1$) a theoretical formulation based on classical mechanical description of charged-particle scattering and neglect of degeneracy is adequate.

The xenon plasma calculations are a useful guide in characterizing the plasma regimes encountered in typical explosive-driven MHD power sources. The length scales and dimensionless parameters have been evaluated on the basis of calculated equilibrium thermodynamic properties of a 10 kbar, 8.5 km/sec xenon plasma, and are shown in Tables 3.2 and 3.3. We have computed the Debye length (D), plasma parameter (Λ) and number of charged particles in the Debye sphere (N_D) in two ways: accounting for both ions and electrons (subscript "c") and accounting for the electrons only (subscript "e"), and this would identify the differences

AD-A079 551

ARTEC ASSOCIATES INC HAYWARD CALIF
EXPLOSIVE MHD RESEARCH, (U)
MAY 77 S P GILL, D W BAUM, W L SHIMMIN
FR-119

F/G 10/2

UNCLASSIFIED

N00014-75-C-0822
NL

20F2
AD
A079551



TABLE 3.2

CALCULATED PLASMA LENGTH SCALES FOR 10 KBAR
XENON DRIVER CONDITIONS

	<u>Ideal Plasma</u>	<u>Debye Huckel</u>
Debye Length with Ion Shielding, Å	3.50	2.76
Debye Length without Ion Shielding, Å	5.99	4.90
Electron DeBroglie Wavelength, Å	.867	.933
Electron Separation, Å	10.9	9.98
Impact Parameter, Å	1.76	2.26

TABLE 3.3
 CALCULATED DIMENSIONLESS PLASMA PARAMETERS
 FOR 10 KBAR XENON DRIVER CONDITIONS

	<u>Ideal Plasma</u>	<u>Debye-Huckel</u>
Interaction Parameter γ	.565	.783
Plasma Parameter		
With Ion Shielding Λ_c	1.99	1.22
Without Ion Shielding Λ_e	3.41	2.17
Charged Particles in Debye Sphere		
Ions and Electrons N_{D_e}	.222	.136
Electrons Only N_{D_e}	.168	.496
Degeneracy Parameter χ_e/r_e	.0798	.0935
Quantum Scattering Parameter χ_e/D_e	.248	.338

resulting from the choice of shielding model used.

The results indicate that the plasma is strongly nonideal, with an important quantum mechanical contribution to charged-particle scattering and with a significant electron degeneracy effect. It is quite clear that the use of any theory such as the Debye-Huckel or the ion-sphere (or an interpolation between the two) that does not account for both types of quantum mechanical effects will not yield a satisfactory description of the equilibrium thermodynamic properties of the plasmas occurring in explosively-driven MHD power sources.

3.5 Survey of Current Research in Nonideal Plasmas

In this section, we will summarize developments in research on equilibrium thermodynamic properties and electrical conductivity of nonideal plasmas published during the last decade. A selected number of prior efforts will be also discussed in order to place the more recent work in perspective.

3.5.1 Equilibrium Thermodynamic Properties

We have tabulated a list of publications relating to the determination of equilibrium thermodynamic properties of nonideal plasmas in Table 3.4, corresponding to References 3.2 to 3.23. Perhaps the most important contribution among these is the exhaustive review of strongly nonideal plasmas

TABLE 3.4

SUMMARY OF RESEARCH ON THERMODYNAMICS OF NONIDEAL PLASMAS

1952	Berlin & Montroll	USA	Classical statistical-mechanical treatment of electrolyte solutions. They show that Debye-Huckel theory is the first order term of a more general theory. Establishes classical limit of applicability of Debye-Huckel theory.
1962	Griem	USA	General formulation for multiply-ionized plasma taking into account Debye-Huckel corrections to ideal gas theory.
1964	McChesney	U.K.	Review of existing techniques for determining reduction of the ionization potential in a plasma.
1965	Vedenov	USSR	Review of thermodynamics of weakly nonideal plasmas.
1966	Stewart & Pyatt	USA	Theory of pressure ionization, based on a finite-temperature Thomas Fermi model, which yields the ion-sphere and Debye-Huckel results as approximate limiting cases.
1966	Van Thiel & Alder	USA	Use of a reflected-shock technique to achieve shock compression of liquid Ar to 700 kbar, 13,000° K.
1966	Brush et al	USA	Monte Carlo study of the thermodynamic properties of a model plasma consisting of heavy ions immersed in a uniform neutralizing background for $0.03 < \gamma < 100$.
1968	Norman & Starostin	USSR	Obtained conditions for the thermodynamic stability of a plasma and showed that for a dense plasma, quantum effects must be taken into account.
1968	Ross	USA	Shock compression of liquid Ar and Xe to 500 kbar and 18,000° K.
1968	Pichakchi	USSR	Theoretical calculation of thermodynamic properties of a dense plasma with less than one particle in the Debye sphere.

TABLE 3.4 (Continued)

1970	Rakhimov & Ulinich	USSR	General considerations relating to thermodynamics of strongly nonideal plasmas.
1970	Vorobev, Norman & Filinov	USSR	Statistical theory of a strongly nonideal, nondegenerate plasma taking account of quantum effects by means of a pseudopotential. Monte Carlo calculations for hydrogen plasma.
1970	Norman & Starostin	USSR	Review of thermodynamics of a strongly nonideal plasma.
1971	Ermokhin	USSR	Based on experimental observation of coulomb diffusion cross-sections for a cesium plasma, suggests a semi-empirical approach for nonideal plasmas consisting of interpolation between Conwell and Weisskopf's theory of semiconductors and ideal plasma theory.
1971	Lomakin & Fortov	USSR	X-ray studies of shock waves in dense cesium vapor.
1971	Fortov	USSR	Calculation of thermodynamic properties of nonideal Cs plasma using a variety of theoretical approaches.
1972	Lomakin & Fortov	USSR	Experimental determination of the equation of state of a nonideal cesium plasma.
1972	Zelener et al	USSR	Statistical theory of nonideal plasmas.
1973	Rogers & DeWitt	USA	Quantum statistical mechanical formulation for equations of state of coulomb gases.
1973	Zelener et al	USSR	Thermodynamic and correlations functions of weakly nonideal non-Debye coulomb systems.

TABLE 3.4 (Continued)

1975	Zelener et al	USSR	Equations of state and ionization equilibrium of nonideal plasma.
1975	Zelener et al	USSR	Deviations of pseudopotential model for nonideal plasma from exact quantum statistics.

by Norman and Starostin (Reference 3.14). This review, published in 1970, covered state of the art thermodynamic property calculation techniques for both weakly nonideal ($\gamma \ll 1$) and strongly nonideal plasmas ($\gamma \geq 1$). Various questions in nonideal plasma theory are discussed, including the inadequacy of classical models, quantum diffraction effects, electron degeneracy, phase transitions and thermodynamic stability.

It is noted that classical approaches such as the Debye-Huckel based on classical statistical mechanics (Reference 3.1), become increasingly inaccurate as the interaction parameter, γ , increases beyond about 0.1. In this regime (which includes explosively driven plasmas) it is necessary to take into account quantum mechanical effects, such as diffraction and electron exchange effects in charged particle collisions and, when the electron number density is sufficiently high, electron degeneracy effects. Only by appropriately accounting for such quantum mechanical effects can thermodynamic stability be guaranteed and phenomena such as phase transitions and plasma metallization be correctly treated.

It is noteworthy that prior to the late 1960's the important advances in research on thermodynamics of nonideal plasmas was predominantly of U. S. origin. The emphasis during this period was on weakly nonideal plasmas relevant

to re-entry type of plasma environment. In more recent years the situation has changed remarkably and in contrast to the paucity of effort in the U. S. and other western nations, the Soviet Union appears to be engaged in a determined effort to understand strongly nonideal plasmas.

This vigorous Soviet effort has been directed towards both theoretical and experimental studies and a concomitant emphasis on the derivation of useful semi-empirical results. The Soviet theoretical work is being pursued primarily by Norman's group, and it is useful to summarize the status of their theoretical effort:

1. Because of the lack of a suitable small parameter in the nonideal plasma regime, it is necessary to rely on involved numerical approaches such as the Monte Carlo method for a theoretical solution of the quantum statistical mechanical description of strongly nonideal plasmas.

2. The fundamental problem is the choice of charged-particle interaction laws that effectively account for quantum effects in a nonideal plasma. The Soviets have devoted a great deal of effort to devising a "pseudopotential" which correctly accounts for quantum mechanical effects in short-range collisions but at the same time reproduces the coulomb potential at large distances.

3. Most of the theoretical studies so far have been for model plasmas without taking account of degeneracy. The plasma model most commonly chosen is one in which the atoms are treated separately as an ideal gas co-existing in ionizational equilibrium with a nonideal subsystem composed of the ionic constituents and free (continuous spectrum) electrons. The interaction of the ions with the continuous-spectrum electrons is described by means of the pseudopotential.

4. Using the Monte Carlo method, the equation of state and ionization equilibrium of the model plasma are computed over a wide range of γ . Results from experimental studies (e.g. Reference 3.18) of nonideal plasmas are being used to estimate undetermined parameters in the pseudopotential and to aid in derivation of similarity laws.

One important U. S. contribution in recent years is that by Rogers and DeWitt (Reference 3.20) who have developed a quantum statistical-mechanical formulation for the equations of state of coulomb gases. However, this approach requires extensive numerical computations and, within the framework of a number of severe approximations, has so far only been applied to the determination of the equation of state of gaseous hydrogen. It is interesting to note that in the hydrogen plasma calculations, the Debye-Huckel relations

are found to be adequate for densities not exceeding 10^{-3} gm/cm³.

In conjunction with a strong theoretical effort, the Soviets have and are continuing a vigorous experimental program. As mentioned above, experimental data is needed for determination of undetermined parameters in the theoretical model. Experimental data is also valuable in developing semi-empirical expressions.

A great deal of the experimental effort has concerned cesium because of the relative ease with which strongly non-ideal plasma conditions can be obtained. Fortov (Reference 3.17) has considered a large number of existing methods for computing the thermodynamic properties of a nonideal cesium plasma and computed these properties for pressures and temperatures in the range 5-150 atm. and 3,000 to 15,000° K (the largest value of γ is 1.08 in this range). His results indicate striking differences in the results obtained by the different theories.

This result illustrates the importance of satisfying oneself that the approach used in thermodynamic calculations is appropriate to the plasma regime of interest, particularly if one is interested in reliable computations for the electrical conductivity which is strongly dependent on thermodynamic properties such as temperature, electron density and average ionic charge.

Ermokhin (Reference 3.15) has conducted experiments with cesium under conditions such that N_D , the number of particles in the Debye sphere varies from about 0.6 to 450. He has shown that the effect of coulombic interaction in this regime is such that a fairly reliable description is obtainable if one interpolates between the weakly nonideal Chapman-Enskog approach for large N_D and the theory of electron interactions with impurity ions in a semiconductor (Reference 3.40) valid for $N_D \ll 1$.

Experiments with inert gases such as xenon and argon which are of direct interest to us, have been comparatively limited and usually not under the conditions of very strong nonidealities explored in cesium plasmas. This is probably because of the experimental difficulties in producing strong nonidealities in these gases.

3.5.2 Electrical Conductivity

A review of the literature on methods for calculating electrical conductivity of a fully ionized nonideal plasma is given in Table 3.5, corresponding to References 3.24 to 3.38.

Historically, rigorous kinetic theory approaches to the calculation of the electrical conductivity have been based on the Chapman-Enskog type of approximations to the collision integral in the Boltzman equation. This approach works well

TABLE 3.5

SUMMARY OF RESEARCH ON ELECTRICAL CONDUCTIVITY OF NONIDEAL PLASMAS

1962	Spitzer	USA	Numerical solution of the Fokker Plank equations for a fully ionized plasma based on assumption of $\Lambda \gg 1$
1965	Ahtye	USA	Review of existing state of the art for conductivity calculations. Development of a second-order Chapman-Enskog solution of the Boltzmann equation.
1967	Mason et al	USA	Numerically evaluated (classical) (Chapman-Enskog) transport collision integrals for the screened coulomb potential.
1967	Robinson	USA	Measurement of conductivity, temperature and energy density at pressures from 3 to 120 kbar in plasmas generated by capacitor discharges in water.
1969	Williams & DeWitt	USA	Asymptotic solution of the quantum-mechanical formulation of plasma transport processes. Approach breaks down if $\Lambda \approx 3$
1970	Bakeev & Rovinskii	USSR	Measurement of electrical conductivity of argon and xenon in a pulsed discharge under conditions such that $2.6 \leq \Lambda \leq 3.3$
1970	Rogov	USSR	Theory of conductivity of fully ionized plasma based on fourth-order Chapman-Enskog approximation to solve the Boltzmann equation. Quantum collisional effects approximately accounted for through use of the Born approximation. Simple analytical results for high-temperature limit.
1971	Batenin & Minaev	USSR	Arc measurement of conductivity of argon and mercury. Results show strong deviation from modified Spitzer-Harm theory starting at $\Lambda \approx 4$

TABLE 3.5 (Continued)

1972	Rovinskii	USSR	Considers semi-empirical methods for electrical conductivity of weakly nonideal ($\gamma \sim 0.1$) plasmas.
1972	Barolskii et al	USSR	Measurement of conductivity of strongly nonideal cesium plasma (γ up to 3).
1973	Devoto	USA	Calculations of conductivity of argon to 1000 atm and 26,000° K using Debye-Huckel thermodynamics and Boltzmann collision operator with the shielded coulomb potential.
1973	Kaklyugin & Norman	USSR	Theory of electrical conductivity for nonideal plasmas assuming a Lorentz gas and accounting for spatial correlation of the charged particles.
1974	Litvinov	USSR	Development of semi-empirical approach for conductivity of nonideal plasma. Effect of degeneracy discussed.
1975	Andreev & Gavrilova	USSR	Measurement of conductivity of air plasma above 100 atmospheres pressure.
1975	Mitin	USSR	Measurement of conductivity of argon and copper in a pulsed arc at conditions corresponding to $1.6 \leq \beta \wedge \leq 3$. Finds Spitzer theory in agreement with measurements. Develops ad hoc semi-empirical improvement of Spitzer expression.

for dilute neutral gases and can be applied to plasmas providing some sort of shielding is applied to the coulomb potential to prevent the long range divergence induced by the pure coulomb potential. Usually the potential is "cut off" at the Debye length or one uses a shielded coulomb potential in which the Debye length is the characteristic shielding distance. An equivalent approach is to consider the Fokker-Planck equation. For fully ionized plasmas, the classic electrical conductivity expression is that of Spitzer-Harm (Reference 3.24) which provides a simple expression valid provided $\ln \Lambda \gg 1$. There have been several efforts to increase the range of applicability of this approach based on both the classical Boltzman equation technique (Reference 3.41) and on quantum mechanical plasma transport theory (Reference 3.28). However, none of these approaches extend the region of applicability to better than $\Lambda \cong 3$ and are thus not appropriate for strongly nonideal plasmas.

The problem arises from the inadequacy of the classical collision models used by all these approaches since, under conditions of strong nonideality, quantum mechanical short range collision effects make an important contribution to the transport integrals. An approximate quantum mechanical approach has been developed by Rogoff (Reference 3.30) who uses a Born approximation with the Debye-shielded potential within the framework of a fourth-order Chapman-Eskog approx-

imation for a fully ionized plasma. Moreover, his results are expressible in terms of a simple analytical expression in the high temperature limit. This result is clearly of great value under conditions of small values of Λ where the classical collision techniques based on the Boltzman equation break down dramatically. However we do not yet have a reliable indication of the accuracy of this method.

A more accurate theory of electrical conductivity for nonideal plasmas has been published by Kaklyugin and Norman (Reference 3.35) who, starting from a Lorentz model with a screened potential, develop an approach that accounts for the spatial correlation of the colliding charged particles. This latter fact, not accountible in the Boltzman transport equation approach, leads to a reduction of the calculated conductivity. This is a result of the localization of some of the free electrons that is accounted for in this approach. Within the context of a model plasma (singly-ionized, non-degenerate) they are able to devise limiting scaling laws that express the ratio σ/σ_0 as a function of the number of particles (N_D) in the Debye sphere (σ_0 is the ideal-gas conductivity valid if $N_D \gg 1$). This is clearly a valuable piece of work, though as published it assumes a somewhat idealized system as compared to the real situation namely: neglect of degeneracy, assumption of a singly ionized plasma etc.

The results of recent Soviet experimental efforts to determine electrical conductivity present some ambiguities that need to be resolved. Batenin and Minaev (Reference 3.31) conclude on the basis of arc measurements in argon and mercury that modified versions of the Spitzer theory (Reference 3.41) which are supposed to be valid down to $\Lambda \approx 4-6$, show serious discrepancies from the measured results starting at $\ln \Lambda = 4$ ($\Lambda \approx 55$). On the other hand Mitin (Reference 3.38) working with argon and copper in pulsed arcs find Spitzer conductivity results to be adequate even for

$\ln \Lambda = 1.6$. Mitin also suggests an interesting semi-empirical modification of Spitzer conductivity formula based on the following changes: (1) replace Λ by $(1 + \Lambda^2)^{1/2}$, and (2) define $\Lambda = n_e^{-1/2} / \bar{b}$ in place of the usual $\Lambda = D / \bar{b}$ for cases where $n_e^{-1/2} > D$.

3.6 Conclusions of Theoretical Program

The approximate values of characteristic plasma parameters have been established by applying ideal plasma theory and the Debye-Huckel theory of weakly nonideal plasma to a nominal explosive driver condition: 10 kbar xenon driver with 8.5 km/sec piston velocity. From a review of the recent literature on nonideal plasmas together with these preliminary calculations we have come to the following conclusions:

1. Plasma produced by an explosive driver is moderately to strongly nonideal, with interaction parameter γ of order unity.

2. The thermodynamics and electrical conductivity of moderately and strongly nonideal plasmas are not well understood at present.

3. The theories applicable to ideal and weakly nonideal plasmas can not be extrapolated to treat the moderately and strongly nonideal gases. Quantum effects play a dominant role in such regimes and only theories that take adequate account of these effects (diffraction and exchange effects in close-range scattering and electron degeneracy effects) will give meaningful results. This is particularly true for strongly nonideal plasmas where quantum effects are needed for guaranteeing thermodynamic stability and proper treatment of phase-transition phenomena, including plasma metallization.

4. The Soviets are currently conducting an aggressive and wide-ranging effort to resolve these problems in nonideal plasmas. Their approach covers three major areas: (1) a strong effort in basic theoretical formulation and numerical computation; (2) a variety of experiments to obtain valid data in nonideal plasma regimes; and (3) the formulation of

semi-empirical techniques to provide useful predictive methods in nonideal plasmas.

5. Most of the published Soviet work has been based on a model plasma -- a singly ionized, nondegenerate system -- and their results must be extended to include multiple ionization and incipient degeneracy effects for explosively driven plasmas.

3.7 Preliminary Estimates of Explosive Plasma Conductivity

Using estimated thermodynamic properties reported in previous sections, we have made preliminary estimates of the electrical conductivity of xenon at a nominal explosive driver condition of 8.5 km/sec flow velocity and 10 kbar pressure. For these calculations we have used three techniques that are applicable to multiply-ionized plasmas and enable rapid computation of the conductivity from the simple analytical expressions given below:

A. Spitzer-Harm Theory (Reference 3.24)

$$\sigma = 329.0 T^{3/2} \alpha(Z) / Z \ln \Lambda_c \text{ (mho/cm)} \quad (3.21)$$

where α is a tabulated function depending on the average ionic charge $Z (= n_e^{-1} \sum_i Z_i^+ n_i)$ and T is expressed in eV.

B. Spitzer-Harm-Mitin Theory (Reference 3.38)

Same as above with following modifications: a) Λ_c replaced by $(1 + \Lambda_c^2)^{1/2}$; and b) average charged particle separation r_c exceeds the Debye length D_c then the plasma parameter is redefined: $\Lambda_c = r_c / \bar{b}_0$ in place of the usual definition $\Lambda_c = D_c / \bar{b}_0$.

C. High Temperature Limit of Rogov's Theory (Reference 3.30)

$$\sigma = 96.97 T^{3/2} \beta(z) / Z \ln \Lambda_R \quad (3.22)$$

where $\Lambda_R = 2D_c / \bar{\lambda}_e$. β , like α in Spitzer's expression above, is a tabulated function of the average ionic charge Z .

Values of conductivities calculated using these three methods are shown in Table 3.6. Thermodynamic properties evaluated using both the ideal-gas assumption and the Debye-Huckel theory without ionic shielding have been used for each conductivity technique. The results are seen to be strongly dependent on the particular conductivity theory chosen and especially noteworthy is the order of magnitude discrepancy exhibited between the prediction based on the Spitzer-Harm theory and that of Rogov's limiting expression (for the Debye-Huckel thermodynamics case).

TABLE 3.6
PRELIMINARY ESTIMATES OF ELECTRICAL CONDUCTIVITY
10 KBAR XENON DRIVER

	<u>Ideal Plasma Approximation</u>	<u>Debye-Huckel without Ion Shielding</u>
Spitzer-Harm	1920 mho/cm	4886 mho/cm
Spitzer-Harm-Mitin	1439	1237
Rogov	529	435

Keeping in mind that experimental measurements of conductivity for this particular plasma condition (xenon, 10 kilobar, 8.5 km/sec) in an imploding cylinder device yielded values in the range of 300-340 mho/cm, we can make the following observations:

(1) The Spitzer-Harm theory is totally inapplicable to the calculation of electrical conductivity at typical explosive driver plasma conditions. This conclusion is not surprising in view of the fact that the Spitzer-Harm theory assumes a classical model for charged particle collisions and furthermore represents an asymptotic solution valid for $\ln \Lambda \gg 1$.

(2) Ad hoc modifications of the Spitzer-Harm theory such as those proposed by Mitin are likely to be only of limited usefulness at plasma conditions of interest to us.

(3) Rogov's theory shows considerable promise as a rapid method for estimating conductivities at explosive driver conditions. This approach is based on a fourth-order Chapman-Enskog solution of the Boltzmann equation. However, in place of a classical model for charged-particle collisions used in the Spitzer-Harm theory and the various modifications applied to it (Reference 3.41), Rogov uses an approximate quantum-mechanical collision model based on the

Born Approximation. The striking improvement in agreement with experimental measurements exhibited by Rogov's theory clearly establishes the importance of accounting for quantum mechanical collisional effects in the theoretical description of the plasma.

(4) Rogov's theory is, however, not rigorous. Firstly, it treats the quantum collisional effects in only an approximate fashion. Secondly, because it is based on the Boltzmann transport equation approach, it fails to allow for various important effects associated with the nonideal behavior of the plasma. For example it neglects the possibility of spatial correlation of the charged particles which, as pointed out by Kaklyugin and Norman (Reference 3.35) may lead to localization of some of the free electrons in a nonideal plasma and thereby tend to lower the conductivity. In view of these limitations, it is clearly necessary to make a careful study of the limits of applicability of the Rogov theory. There is undoubtedly considerable scope for improvement of this theory to the point where it could be relied upon as an accurate predictor of conductivity over most if not all of the plasma parametric regime of interest in explosive driver development. Clearly, concurrent experimental efforts toward obtaining accurate conductivity measurements would greatly aid the achievement of this important goal.

4. CONCLUSIONS AND RECOMMENDATIONS

4.1 Summary of Program Accomplishments

1. Experiments were successfully performed using three explosive driver types (imploding cylindrical, exploding cylindrical, and disc) and two gases (argon and xenon).

2. Plasma diagnostic data was successfully obtained using an MHD velocity gage, an eddy current plasma conductivity gage, plasma resistance measurements, an optical pyrometer, and shock wave instrumentation.

3. A literature survey on nonideal plasma theory and data was carried out, and considerable insight was gained regarding the physics of explosively driven plasmas.

4. Preliminary calculations of plasma conductivity using several theoretical models were carried out and compared with experimental data. The results demonstrate the importance of nonideal plasma phenomena, and provide encouraging progress in removing the discrepancy between experiment and theory.

4.2 Recommendations

1. Further experimental work needs to be performed to provide an adequate data base on electrical conductivity,

temperature, and other accessible parameters of explosively driven plasmas.

2. Experimental and theoretical work should be performed on ablation and boundary layer growth in explosively driven plasmas, with particular attention paid to electrical conductivity and velocity gradients in the plasma.

3. To provide accurate experimental data further diagnostic development work must be performed. In particular three-dimensional MHD calculations should be performed to investigate the conductivity averaging process in the eddy current conductivity gage and plasma resistance measurement. Additional effort to reduce nonideal effects in the explosive driver would also improve accuracy. Some development of the optical pyrometer is necessary to obtain absolutely calibrated data.

4. Further work is required to develop the theory of nonideal plasmas to the point where useful predictions of experimental environments can be made.

REFERENCES

- 1.1 Gill, S. P. et al, "Explosive MHD Research", Artec Associates Inc. Annual Report 119AR, Navy Contract N00014-75-C-0822, April 1976.
- 1.2 Baum, D. W. et al, "Development of High Energy Density Simulator", Artec Associates Inc. Final Report 120, Defense Nuclear Agency Contract DNA001-75-C-0271, December 1976.
- 1.3 Baum, D. W. et al, "Explosive MHD Power Source", Artec Associates Inc. Final Report 113, Navy Contract N00178-75-C-0120, June 1977.
- 3.1 Zeldovich, Ya. B and Raizer, Yu. P., "Physics of Shock Waves and High Temperature Hydrodynamic Phenomena", Academic Press, New York, 1966.
- 3.2 Berlin, T. H. and Montroll, E. W., "On the Free Energy of a Mixture of Ions: An Extension of Kramer's Theory", J. Chem. Phys., 20, 1952, p. 75.
- 3.3 Griem, H. R., "High Density Corrections in Plasma Spectroscopy", Phys. Rev., 128, 1962, p. 997.
- 3.4 McChesney, M., "Equilibrium Shockwave Calculations in Inert Gas, Multiply-Ionized Debye-Huckel Plasmas", Can. J. Phys., 42, 1964, p. 2473.
- 3.5 Vedenov, A. A., "Thermodynamics of a Plasma", Reviews of Plasma Physics, Vol. 1, Consultants Bureau, New York, 1965, p. 312.
- 3.6 Stewart, J. C. and Pyatt, K. D., "Lowering of the Ionization Potential in Plasmas", Astrophys. J. 144, 1966, p. 1203.
- 3.7 Van Thiel, M. and Alder, B. J., "Shock Compression of Argon", J. Chem. Phys., 44, 1966, p. 1056.
- 3.8 Brush, S. G. et al, "Monte Carlo Study of a One-Component Plasma", J. Chem. Phys., 45, 1966, p. 2102.
- 3.9 Norman, G. E. and Starostin, A. N., "Insufficiency of the Classical Description of a Nondegenerate Dense Plasma", Tepl. Vys. Temp., 6, 1968, p. 410.

- 3.10 Ross, M., "Shock Compression of Argon and Xenon IV: Conversion of Xenon to a Metal-like State", Phys. Rev., 171, 1968, p. 777.
- 3.11 Pichakchi, L. D., "The Thermodynamics of a Dense Plasma", Sov. Phys. JETP, 26, 1968, p. 845.
- 3.12 Rakhimov, A. T. and Ulinich, F. R., "The Possibility of Existence of a Strongly Nonideal Plasma", Sov. Phys. JETP, 30, 1968, p. 772.
- 3.13 Vorob'ev, V. W., et al, "Statistical Theory of a Dense Plasma", Sov. Phys. JETP, 30, 1970, p. 459.
- 3.14 Norman, G. E. and Starostin, A. N., "Thermodynamics of a Strongly Nonideal Plasma", Tepl. Vys. Temp., 18, 1970, p. 413.
- 3.15 Ermokhin, N. V. et al, "An Experimental Investigation of Coulomb Interaction in a Dense Plasma", Tepl. Vys. Temp., 9, 1971, p. 665.
- 3.16 Lomakin, B. N. and Fortov, V. E., "Pulsed X-ray Studies of Shockwaves in Dense Cesium Vapor", Tepl. Vys. Temp., 9, 1971, p. 1291.
- 3.17 Fortov, V. E. et al, "Thermodynamic Properties of a Cesium Plasma", Tepl. Vys. Temp., 9, 1971, p. 869.
- 3.18 Lomakin, B. N. and Fortov, V. E., Zh. Eksp. Fiz., 63, No. 7. 1972.
- 3.19 Zelener, B. V. et al, "Statistical Theory of a Nonideal Plasma", Tepl. Vys. Temp., 10, 1972, p. 1160.
- 3.20 Rogers, F. J. and Dewitt, H. E., "Statistical Mechanics of Reacting Coulomb Gases", Phys. Rev. A, 8, 1973, p. 1061.
- 3.21 Zelener, B. V. et al, "Thermodynamics and Correlation Function of Weakly Nonideal Non-Debye Coulomb Systems", Tepl. Vys. Temp., 11, 1973, p. 922.
- 3.22 Zelener, B. V. et al, "Equations of State and Ionization Nonequilibrium of a Nonideal Plasma", Tepl. Vys. Temp., 13, 1975, p. 913.
- 3.23 Zelener, B. V. et al, "Pseudopotential Model of a Nonideal Plasma", Temp. Vys. Temp., 13, 1975, p. 712.

- 3.24 Spitzer, L., "Physics of Fully Ionized Gases", Wiley Interscience, 2nd Edition, 1962.
- 3.25 Ahtye, W. F., "A Critical Evaluation of Methods for Calculating Transport Coefficients of Partially and Fully Ionized Gases", NASA TN-D 2611, January 1965.
- 3.26 Mason, E. A. et al, "Transport Coefficient of Ionized Gases", Phys. Fluid, 10, 1967, p. 1827.
- 3.27 Robinson, J. W., "Measurement of Plasma Energy Density and Conductivity from 3 to 120 kbar", J. Appl. Phys. 38, 1967, p. 210.
- 3.28 Williams, R. H. and Dewitt, H. W., "Quantum Mechanical Plasma Transport Theory", Phys. Fluid, 12, 1969, p. 2326.
- 3.29 Bakeev, A. A. and Rovinsky, R. E., "Electrical Properties of High-Pressure Pulsed Discharge Plasma in Inert Gases", Tepl. Vys. Temp., 8, 1970, p. 1121.
- 3.30 Rogoff, V. S., "Calculation of Plasma Conductivity", Tepl. Vys. Temp., 8, 1970, p. 689.
- 3.31 Batenin, V. M. and Minaev, D. V., Tepl. Vys. Temp., 9, 1971, p. 676.
- 3.32 Rovinskii, R. E., "Electrical Conductivity of a Non-Debye Plasma", Tepl. Vys. Temp., 1972, p. 1.
- 3.33 Barolskii, S. G. et al, "Measurement of the Electrical Conductivity of a Dense Strongly Nonideal Cesium Plasma", Sov. Phys. JETP, 35, 1972, p. 94.
- 3.34 Devoto, R. S., "Transport Coefficients of Ionized Argon", Phys. Fluid, 16, 1973, p. 616.
- 3.35 Kaklyugin, A. S. and Norman, G. E., "Electrical Conductivity of a Non-Debye Plasma", Tepl. Vys., Temp., 11, 1973, p. 238.
- 3.36 Litvinov, I. I., "Electrical Conductivity of a Non-Debye Plasma", Tepl. Vys. Temp., 13, 1974, p. 1100.
- 3.37 Andreev, S. and Gavrilova, T. V., "Measurement of Electrical Conductivity of Air Plasma at Pressures Above 100 atm.", Templ. Vys. Temp., 13, 1975, p. 176.

- 3.38 Mitin, R. B., "Experimental Determination of the Electrical Conductivity of Dense Plasmas with Low Coulomb Logarithm", Tepl. Vys. Temp., 13, 1975, p. 706.
- 3.39 Ecker, G. and Kroll, W., "Lowering of the Ionization Potential for a Plasma in Thermodynamic Equilibrium", Phys. Fluid, 6, 1962, p. 62.
- 3.40 Conwell, E. M. and Weisskopf, V. F., Phys. Rev., 77 1950, p. 388.
- 3.41 Kruger, C. H. et al, "Transport Properties of MHD Generator Plasmas", AIAA J., 6, 1968, p. 1712.